

On molecular transport effects in real gas laminar diffusion flames at large pressure

Sridhar Palle, Christopher Nolan, and Richard S. Miller^{a)}

Department of Mechanical Engineering, Clemson University, Clemson, South Carolina 29634-0921

(Received 31 August 2004; accepted 31 May 2005; published online 11 October 2005)

Direct numerical simulations are conducted of unsteady, exothermic and one-dimensional laminar diffusion flames at large pressures. The simulations are used to assess the impact of molecular diffusion and real gas effects under high pressure conditions with simplified chemical kinetics. The formulation includes the fully compressible form of the governing equations, real gas effects modeled by the cubic Peng–Robinson equation of state, and a generalized form of the Soret and Dufour mass and heat diffusion vectors derived from nonequilibrium thermodynamics and fluctuation theory. The cross diffusion fluxes are derived for a ternary species system and include the effects of both heat and mass diffusion in the presence of temperature, concentration and pressure gradients (i.e., Soret and Dufour diffusion). The ternary species formulation is applied to a simplified single step reaction elucidating molecular and thermodynamic effects apparent in general combustion. Realistic models for pressure, temperature and species dependent heat capacities, viscosities, thermal conductivities and mass diffusivities are also included. Three different model reactions are simulated both including and neglecting Soret and Dufour cross diffusion. The simulation results show that Soret and Dufour effects are negligible for reactions comprised of species with equal or near equal molecular weights. However, Soret diffusion effects are apparent when species with nonequal molecular weights are involved in the reaction and result in reductions of the peak flame temperature. In addition, it is shown that neglect of cross diffusion leads to deviations in the predicted flame thicknesses, with under predictions for a hydrogen-oxygen system and over predictions for a heavy hydrocarbon reaction. These effects are explained in detail through examinations of the individual heat and mass flux vectors as well as through associated thermodynamic properties. A parametric study addresses the effects of the ambient pressure, the initial “flame Reynolds number,” the Damkohler number and the heat release parameter. © 2005 American Institute of Physics. [DOI: 10.1063/1.1990198]

I. INTRODUCTION

The following study is motivated by the supercritical fuel injection and cylinder pressures encountered in modern combustion technologies, including, power and aircraft turbines,¹ diesel engines² and rocket engines. High pressure fluid flow may be characterized as either supercritical or subcritical with respect to a species' critical temperature and/or pressure (the critical “locus” for a mixture).³ Above the critical conditions there is no distinction between gaseous and liquid phases and the supercritical flow state is generally referred to simply as “fluid.” In fact, under supercritical pressures the distinction between phases (including latent heats and surface tension) vanishes, and both the terms “droplet” and “vaporization” are no longer applicable. We also note that for present purposes the term “supercritical” is used whenever either the pressure or the temperature of the fluid (or mixture) is fixed above its critical point (or locus) since in either case there is no possibility for phase change. Although the lack of phase change somewhat simplifies the purely supercritical flow analysis by alleviating effects of phase boundaries, surface tension, and latent heat, very high

pressure fluid mixing and combustion are found to generally require the inclusion of a real gas equation of state (EOS) and corresponding real gas thermodynamic functions such as enthalpy, heat capacity, acoustic speed, etc.

In progressing to high pressure combustion modeling many effects must be considered, including, pressure induced modifications to chemical kinetics, reaction mechanisms,⁴ turbulence modeling, “atomization” of “liquid” fuels, and radiation modeling (due to greatly increased fluid densities). Each of these effects deserve substantial research, however, the subject of the present work is on the additional impacts of the molecular transport model, real gas effects (through the EOS), and property modeling. “Irreversible” or “nonequilibrium”⁵ thermodynamic effects have been shown to be important under certain high pressure conditions (see below). These molecular transport effects from which species concentrations diffuse due to temperature or pressure gradients (Soret effect, or “thermal-diffusion”) and thermal energy diffuses due to concentration or pressure gradients (Dufour effect, or “diffusion-thermo”) have also been shown to be significant in real fluids at both atmospheric^{6–13} and supercritical^{14–23} pressures, particularly when large ratios of the molecular weights of the pure compounds are present.⁸ Molecular transport effects are important for both non-

^{a)}Telephone: 864-656-6248; Fax: 864-656-4435; Electronic Mail: rm@clemson.edu

premixed and premixed flames as both involve substantial temperature and concentration gradients within the local flame zone. A recent review of (low pressure) combustion simulations reveals that the impact of the chosen molecular diffusion model can be as large as the observed differences between available chemical kinetics models.²⁴ Differences in molecular transport models can result in both variations in observed diffusion rates, as well as alterations to local flame curvature and strain rates.²⁴ In fact, Rosner *et al.*¹² pointedly criticize the seemingly widely held view in the combustion community that Soret diffusion is not important for proper combustion modeling (although the Dufour effect is generally negligible), and offer ample evidence that such effects can indeed be important, even for “heavy” species.

In regard to actual combustion studies which include Soret and Dufour cross diffusion effects, little, if any, work has been done at large pressures. However, several papers have addressed these effects under atmospheric pressure and low Mach number conditions. Greenberg²⁵ simulated an atmospheric hydrogen-air flame and found that thermal diffusion fluxes are comparable in magnitude to the Fickian contributions and recommend that they be incorporated into flame codes. Garcia-Ybarra *et al.*²⁶ performed a theoretical estimation of the influence of Soret and Dufour diffusion on wrinkled premixed flames by assuming a weak cross-diffusion coupling. Under conditions of large activation energy they conclude that Soret mass diffusion cannot be neglected when analyzing flame front dynamics (Dufour effects were found to be negligible). Ern and Giovangigli⁹ numerically simulated two-dimensional (2D) steady laminar methane-air and hydrogen-air diffusion flames using a more complete formulation of the Soret and Dufour fluxes together with complex chemistry and accurate models for transport coefficients. Their very complete formulation still does not include either the mass diffusion factor (implicitly assumed to be unity) or the effects of pressure gradients, both of which would be negligible under the low pressures and low Mach numbers investigated. In agreement with the above theoretical study it was concluded that Soret effects must be considered for accurate flame calculations when the molecular weights of the constituent species substantially vary. For example, in the hydrogen-air flame the Soret contribution to the mass flux vector comprised as much as 50% of the total flux vector magnitude, thereby enhancing the rate of mass diffusion. Important alterations to species concentrations were also observed, including, H, H₂, H₂O₂ and HCO in the methane flame. Finally, Rosner *et al.*¹² and Dakhliya *et al.*¹³ incorporated a similar formulation into their investigations of Soret effects on low pressure air-breathing combustion and laminar counterflow spray diffusion flames; also 2D laminar low speed flow. In addition to confirming earlier findings of the importance of Soret diffusion on “light” species they indicate that even “heavy” species diffusion can be altered by Soret effects. In the region surrounding the droplet flame they measure peak flame temperature Soret-induced reductions as large as 125 K when helium is used as a diluent. Even temperature discrepancies of this order can have substantial impact on pollutant (and other trace species) concentration predictions, as well as on engine fatigue and failure.

Relatively little research exists for high pressure flows including Soret and Dufour diffusion, with the majority only considering binary species, nonreacting flows. Curtis and Farrell⁸ were the first to include cross-diffusion effects in their simulations of supercritical droplets using a derivation containing diffusion due to temperature and concentration, but not pressure, gradients. Since then, Bellan’s group^{14–17} at Jet Propulsion Laboratory (JPL) have simulated high pressure fluid droplet “diffusion” based on a complete derivation of the heat and mass flux vectors for a binary species system derived from nonequilibrium thermodynamics⁵ and fluctuation theory.²⁷ They further included the mass diffusion factor which approaches unity (pure Fickian diffusion) away from the critical locus, but goes to zero at the critical locus yielding infinite effective Schmidt number. This is also the only derivation known to the authors which retains the potential for thermal and mass diffusion in the presence of pressure gradients, as most studies are usually limited to low Mach number flows. Their formulation has also been applied to the direct numerical simulation (DNS) of nonhomogeneous turbulent binary mixing in both 2D and 3D temporally developing mixing layers formed by the merging of supercritical pressure nitrogen/heptane streams,^{18,19} and oxygen/hydrogen streams.²⁸

Despite prior work in nonhomogeneous flows at supercritical pressure, several interesting Soret and Dufour diffusion-induced mixing phenomena are more readily apparent in homogeneous turbulence. Beginning with the binary species formulation of the diffusion fluxes developed at JPL, Miller²⁰ conducted DNS of the mixing of various nitrogen-hydrocarbon mixtures in stationary isotropic compressible turbulence. Simulations were initialized as perfectly premixed binary species systems with 50/50 nitrogen with heptane, 3-methylhexane and dodecane. Unlike a typical low pressure system, the perfectly premixed species were observed to initially “anti-diffuse” due to a Soret cross diffusion induced by pressure gradients present in the compressible flow. A statistically steady scalar state was eventually achieved in each simulation through a balance between the scalar variance production due to the pressure gradient term and the traditional destructive nature of the Fickian diffusion term.

Lou and Miller^{21,22} then considered the impact of Soret and Dufour cross-diffusion effects on mixing and nonexothermic reactions through an examination of the scalar probability density function (PDF) transport equation for binary mixing in isotropic turbulence at supercritical pressure. They conducted DNS of the binary isotropic mixing case at a resolution of 192³ grid points for heptane mixing with nitrogen from initially non-premixed conditions at 45 atm pressure and 700 K mean temperature. Several new terms appearing in the PDF transport equation were identified and observed to be important to the long time scalar evolution. Models typically used for the low pressure PDF transport equation were found to perform poorly at high pressures and long mixing times.

Continuing on to increasingly more realistic reacting flow cases, Lou and Miller^{22,23} derived the complete forms of the Soret and Dufour diffusive fluxes for a ternary species

configuration allowing the simulation of a simplified three species reaction in stationary isotropic turbulence. For the case of reacting flow,^{22,23} a simple nonexothermic reaction of the form $O_2 + N_2 \rightarrow 2NO$ was considered from non-premixed initial conditions.^{22,23} The destruction of two species due to the reaction was observed to yield an eventual binary species state. Therefore, at long times chemically reacting flows again yield stationary scalar states at finite times, however, the time required to reach this state is longer than in the binary species results. This final state is also characterized by stationary scalar variance and by asymmetric scalar PDFs exhibiting exponential tails. Only nonexothermic reactions were considered due to the limitations of isotropic “box” turbulence.

It is clear from the above that significant continuing research is required in order to understand the nature of both Soret and Dufour diffusion and real gas effects on high pressure flames related to modern combustion devices. Particularly lacking from the literature are the effects of large temperature gradients associated with exothermic flames and their potential enhancements of Soret diffusion terms. The objectives of the present investigation are therefore to perform DNS of one-dimensional (1D) laminar diffusion flames under relevant thermodynamic conditions (here the term DNS is used to emphasize that no subgrid modeling is employed and all spatial and temporal scales of the equations are fully resolved). The chosen formulation includes a real gas state equation, generalized thermodynamic diffusion for a ternary species system, and realistic models for the temperature, concentration and pressure dependence of all species properties. Three individual reactions of the form $A + r_1 B \rightarrow r_2 C$ are chosen under the limitations of the ternary species derivation with constant rate exothermic kinetics (fully generalized diffusion including pressure gradient dependent terms has not yet been derived for more than three species systems). Although the reactions are simplified models, real species of relevance to high pressure combustion are used for the species A , B , and C , including detailed property models. All reactions are unsteady in order to examine any potential impact of large early time pressure gradients associated with ignition on the cross diffusion.

A fundamental study is conducted by fixing pertinent nondimensional parameters (the flame Reynolds number, the Damkohler number, and the heat release parameter) and studying the effects of varying these parameters in a parametric study. As such, the particular reactions simulated are not meant to conform to specific real reaction parameters since such a study would require highly detailed kinetics for which the fully generalized cross-diffusion terms have yet to be derived. The present emphasis is on providing the physical understanding of how and why cross diffusion acts under several representative, and tractable, ternary species systems. This information is required before appropriate modeling approaches to more complex and realistic chemically reacting systems can be developed and will potentially aid in the development of such models. For this purpose, all simulations are performed both including and neglecting Soret and Dufour cross diffusion allowing for a parametric assessment of the differences in simulation results including and neglect-

ing these effects. The paper is organized as follows. The formulation is presented in Sec. II, the numerical approach is described in Sec. III, results are presented in Sec. IV and Sec. V contains general conclusions. Specifics of the mixture property models are provided in the Appendix.

II. FORMULATION

The primary objective of the study involves the elucidation of potential molecular transport effects in high pressure reactions involving realistic heat release and associated temperature gradients. Due to the fact that such effects could easily be obfuscated in complex reactions involving many species, and due to the fact that only a ternary species complete derivation of the cross-diffusion fluxes yet exists, we choose to study a relatively simplified chemical reaction of the form $A + r_1 B \rightarrow r_2 C$ with constant rate one-step kinetics. The species A , B , and C denote the two reactant and product species, and r_1 and r_2 are stoichiometric coefficients for the particular reaction. The governing equations for a ternary species system under general supercritical pressure conditions have been presented previously in Refs. 22 and 23 and will therefore only be summarized in what follows. However, the present formulation extends these works through the addition of realistic models for the mixture viscosity, conductivity, and binary diffusivities as functions of temperature, pressure, and concentration.

The general high pressure flow formulation is based on the compressible form of the continuity, momentum, and total energy (internal plus kinetic) equations:

$$\frac{\partial \rho}{\partial t} + \frac{\partial}{\partial x_j} [\rho u_j] = 0, \quad (1)$$

$$\frac{\partial}{\partial t} (\rho u_i) + \frac{\partial}{\partial x_j} [\rho u_i u_j + P \delta_{ij} - \tau_{ij}] = 0, \quad (2)$$

$$\frac{\partial}{\partial t} (\rho e_t) + \frac{\partial}{\partial x_j} [(\rho e_t + P) u_j - u_i \tau_{ij} + Q_j] = -\Delta H_F^0 \dot{\omega}_3, \quad (3)$$

where u_i is the mixture velocity vector, ρ is the mixture density, P is the pressure, δ_{ij} is the Kronecker delta function tensor, τ_{ij} is the viscous stress tensor (assumed Newtonian), e_t is the total specific energy, Q_j is the heat flux vector, $-\Delta H_F^0$ is the heat of reaction, and $\dot{\omega}_3$ is the reaction rate for the product species (species C above). Transport equations for the two reactant mass fractions, denoted species 1 and 2 (Y_1 and Y_2), including reaction terms, are

$$\frac{\partial}{\partial t} (\rho Y_1) + \frac{\partial}{\partial x_j} [\rho Y_1 u_j + J_{j,1}] = \dot{\omega}_1, \quad (4)$$

$$\frac{\partial}{\partial t} (\rho Y_2) + \frac{\partial}{\partial x_j} [\rho Y_2 u_j + J_{j,2}] = \dot{\omega}_2, \quad (5)$$

where $J_{j,\alpha}$ is the mass flux vector for species α . The species 3 mass fraction is evaluated as $Y_3 = 1 - Y_1 - Y_2$. In the formulation species 1, 2, and 3 denote reactant species A , B , and product species C , respectively. Real gas effects are included through the cubic Peng–Robinson EOS:

$$P = \frac{\mathcal{R}T}{V - \mathcal{B}_m} - \frac{\mathcal{A}_m}{V^2 + 2V\mathcal{B}_m - \mathcal{B}_m^2}, \quad (6)$$

where \mathcal{R} is the universal gas constant, T is the temperature, V is the molar volume, and \mathcal{A}_m and \mathcal{B}_m are model constants evaluated through appropriate mixing rules (presented previously in Refs. 20, 22, and 23). This form was chosen due to its relative computational efficiency, relative accuracy over the range of thermodynamic conditions considered, and the availability of a simple correction which substantially increases its accuracy if warranted.²⁹ Finally, the reaction rates for species 1 and 2 are defined as $\dot{\omega}_1 = -\rho^2 K_R Y_1 Y_2 / M_2$ and $\dot{\omega}_2 = -r\rho^2 K_R Y_1 Y_2 / M_1$, where K_R is the reaction rate coefficient (assumed constant for simplicity) and $\dot{\omega}_3 = -\dot{\omega}_1 - \dot{\omega}_2$ as a consequence of the conservation of mass.

A. Heat and mass flux vectors

The heat flux (Q_j) and mass flux ($J_{i,\alpha}$) vector formulation for a ternary species system is derived in Refs. 22 and 23 based on nonequilibrium thermodynamics and Keizer's fluctuation-dissipation theory. Resultant heat and mass flux vectors are repeated here for the sake of clarity and will be referred to in interpreting the forthcoming simulation results. They are presented as superpositions of terms proportional to temperature, concentration, and pressure gradients:

$$Q_j = Q_j^T + Q_j^{Y_1} + Q_j^{Y_2} + Q_j^P, \quad (7)$$

and

$$J_{j,\alpha} = J_{j,\alpha}^{Y_1} + J_{j,\alpha}^{Y_2} + J_{j,\alpha}^T + J_{j,\alpha}^P, \quad (8)$$

where the superscripts indicate the pertinent thermodynamic gradient. Final forms for the heat flux components are

$$Q_j^T = - \left\{ \kappa + \mathcal{R} \frac{M_m^2}{M_1 M_2} Y_1 Y_2 n D_m^{(12)} \alpha_{IK}^{(12)} \alpha_{BK}^{(12)} + \mathcal{R} \frac{M_m^2}{M_1 M_3} Y_1 Y_3 n D_m^{(13)} \alpha_{IK}^{(13)} \alpha_{BK}^{(13)} + \mathcal{R} \frac{M_m^2}{M_2 M_3} Y_2 Y_3 n D_m^{(23)} \alpha_{IK}^{(23)} \alpha_{BK}^{(23)} \right\} \frac{\partial T}{\partial x_j}, \quad (9)$$

$$Q_j^{Y_1} = -n\mathcal{R}T \left\{ Y_2 \alpha_{IK}^{(12)} D_m^{(12)} \alpha_D^{(11)} + Y_1 \alpha_{IK}^{(21)} D_m^{(21)} \alpha_D^{(21)} + Y_3 \alpha_{IK}^{(13)} D_m^{(13)} \alpha_D^{(11)} + Y_1 \alpha_{IK}^{(31)} D_m^{(31)} \alpha_D^{(31)} + Y_3 \alpha_{IK}^{(23)} D_m^{(23)} \alpha_D^{(21)} + Y_2 \alpha_{IK}^{(32)} D_m^{(32)} \alpha_D^{(31)} \right\} \frac{\partial X_1}{\partial x_j}, \quad (10)$$

$$Q_j^{Y_2} = -n\mathcal{R}T \left\{ Y_2 \alpha_{IK}^{(12)} D_m^{(12)} \alpha_D^{(12)} + Y_1 \alpha_{IK}^{(21)} D_m^{(21)} \alpha_D^{(22)} + Y_3 \alpha_{IK}^{(13)} D_m^{(13)} \alpha_D^{(12)} + Y_1 \alpha_{IK}^{(31)} D_m^{(31)} \alpha_D^{(32)} + Y_3 \alpha_{IK}^{(23)} D_m^{(23)} \alpha_D^{(22)} + Y_2 \alpha_{IK}^{(32)} D_m^{(32)} \alpha_D^{(32)} \right\} \frac{\partial X_2}{\partial x_j}, \quad (11)$$

$$Q_j^P = -nM_m \left\{ Y_1 Y_2 \alpha_{IK}^{(12)} D_m^{(12)} \left(\frac{V_{,1}}{M_1} - \frac{V_{,2}}{M_2} \right) + Y_1 Y_3 \alpha_{IK}^{(13)} D_m^{(13)} \left(\frac{V_{,1}}{M_1} - \frac{V_{,3}}{M_3} \right) + Y_2 Y_3 \alpha_{IK}^{(23)} D_m^{(23)} \left(\frac{V_{,2}}{M_2} - \frac{V_{,3}}{M_3} \right) \right\} \frac{\partial P}{\partial x_j}, \quad (12)$$

where X_α is the mole fraction of species α , M_α is the molecular weight of species α , $M_m = \sum X_\alpha M_\alpha$ is the mixture molecular weight, κ is the thermal conductivity consistent with kinetic theory, and κ_{eff} is the "effective" thermal conductivity:

$$\kappa_{eff} = \kappa + \mathcal{R} \frac{M_m^2}{M_1 M_2} Y_1 Y_2 n D_m^{(12)} \alpha_{IK}^{(12)} \alpha_{BK}^{(12)} + \mathcal{R} \frac{M_m^2}{M_1 M_3} Y_1 Y_3 n D_m^{(13)} \alpha_{IK}^{(13)} \alpha_{BK}^{(13)} + \mathcal{R} \frac{M_m^2}{M_2 M_3} Y_2 Y_3 n D_m^{(23)} \alpha_{IK}^{(23)} \alpha_{BK}^{(23)}, \quad (13)$$

i.e., $Q_j^T = -\kappa_{eff} \partial T / \partial x_j$ (note, however, that prior results²⁰ have shown that in general $\kappa_{eff} \approx \kappa$). Continuing, $n = V^{-1}$ is the molar density, $D_m^{(ij)} = D_m^{(ji)}$ are the binary diffusion coefficients between species i and j , and $\alpha_D^{(ij)}$ are the mass diffusion factors. The mole and mass fractions are related through $M_\alpha X_\alpha = M_m Y_\alpha$. The "Irving-Kirkwood" and the "Bearman-Kirkwood" forms of the nondimensional thermal diffusion factors are $\alpha_{IK}^{(ij)}$ and $\alpha_{BK}^{(ij)}$, respectively. These properties of the fluid mixture are discussed below. Finally, the partial molar volume is $V_{,i} = \partial V / \partial X_i$.

The corresponding mass flux vector components for species 1 are

$$J_{j,1}^{Y_1} = -n \frac{M_1}{M_m} \left\{ M_2 Y_2 D_m^{(12)} \alpha_D^{(11)} + M_3 Y_3 D_m^{(13)} \alpha_D^{(11)} - M_2 Y_1 D_m^{(12)} \alpha_D^{(21)} - M_3 Y_1 D_m^{(13)} \alpha_D^{(31)} \right\} \frac{\partial X_1}{\partial x_j}, \quad (14)$$

$$J_{j,1}^{Y_2} = -n \frac{M_1}{M_m} \left\{ M_2 Y_2 D_m^{(12)} \alpha_D^{(12)} + M_3 Y_3 D_m^{(13)} \alpha_D^{(12)} - M_2 Y_1 D_m^{(12)} \alpha_D^{(22)} - M_3 Y_1 D_m^{(13)} \alpha_D^{(32)} \right\} \frac{\partial X_2}{\partial x_j}, \quad (15)$$

$$J_{j,1}^T = -M_m \frac{n}{T} \left\{ Y_1 Y_2 D_m^{(12)} \alpha_{BK}^{(12)} + Y_1 Y_3 D_m^{(13)} \alpha_{BK}^{(13)} \right\} \frac{\partial T}{\partial x_j}, \quad (16)$$

and

$$J_{j,1}^P = -\frac{nM_1}{\mathcal{R}T} \left\{ M_2 Y_1 Y_2 D_m^{(12)} \left(\frac{V_{,1}}{M_1} - \frac{V_{,2}}{M_2} \right) + M_3 Y_1 Y_3 D_m^{(13)} \left(\frac{V_{,1}}{M_1} - \frac{V_{,3}}{M_3} \right) \right\} \frac{\partial P}{\partial x_j}, \quad (17)$$

respectively, whereas those for species 2 are

TABLE I. Molecular weight, critical temperature and pressure, acentric factor, and total atomic diffusion volume for all species considered in the study (Ref. 3).

Species	M	T^C [K]	P^C [atm]	Ω	Σ_v
Nitrogen (N ₂)	28.013	126.26	33.46	0.039	18.5
Oxygen (O ₂)	31.999	154.6	49.74	0.025	16.3
Nitric Oxide (NO)	30.006	180.0	63.95	0.588	10.65
Dodecane (C ₁₂ H ₂₆)	170.34	658.2	17.96	0.575	250.86
Heptane (C ₇ H ₁₆)	100.205	540.3	27.04	0.349	148.26
Hydrogen (H ₂)	2.016	33.2	13.0	-0.218	6.12
Water (H ₂ O)	18.015	647.3	221.2	0.344	13.1

$$J_{j,2}^{Y_1} = -n \frac{M_2}{M_m} \left\{ -M_1 Y_2 D_m^{(12)} \alpha_D^{(11)} + M_1 Y_1 D_m^{(12)} \alpha_D^{(21)} + M_3 Y_3 D_m^{(23)} \alpha_D^{(21)} - M_3 Y_2 D_m^{(23)} \alpha_D^{(31)} \right\} \frac{\partial X_1}{\partial x_j}, \quad (18)$$

$$J_{j,2}^{Y_2} = -n \frac{M_2}{M_m} \left\{ -M_1 Y_2 D_m^{(12)} \alpha_D^{(12)} + M_1 Y_1 D_m^{(12)} \alpha_D^{(22)} + M_3 Y_3 D_m^{(23)} \alpha_D^{(22)} - M_3 Y_2 D_m^{(23)} \alpha_D^{(32)} \right\} \frac{\partial X_2}{\partial x_j}, \quad (19)$$

$$J_{j,2}^T = -M_m \frac{n}{T} \left\{ Y_2 Y_3 D_m^{(23)} \alpha_{BK}^{(23)} - Y_1 Y_2 D_m^{(12)} \alpha_{BK}^{(12)} \right\} \frac{\partial T}{\partial x_j}, \quad (20)$$

and

$$J_{j,2}^P = -\frac{nM_2}{\mathcal{R}T} \left\{ M_1 Y_1 Y_2 D_m^{(12)} \left(\frac{V_{,2}}{M_2} - \frac{V_{,1}}{M_1} \right) + M_3 Y_2 Y_3 D_m^{(23)} \times \left(\frac{V_{,2}}{M_2} - \frac{V_{,3}}{M_3} \right) \right\} \frac{\partial P}{\partial x_j}, \quad (21)$$

respectively. If required, the mass flux vector $J_{j,3}$ can be calculated in mass form based on the conservation principle: $\sum_{\alpha} J_{i,\alpha} = 0$, where the summation is over all three species.

B. Property evaluations

Molecular weights, critical properties, acentric factors, and total atomic diffusion volumes (used for mass diffusivity calculations) for all species considered in this study are presented in Table I.³ Expanding our previous works, the present investigation incorporates models for the realistic temperature, pressure, and concentration dependence of the mixture viscosity (μ), thermal conductivity (κ), and binary mass diffusivities ($D_m^{(ij)}$). Suitable procedures based on the principle of corresponding states for calculating each property were chosen from the literature and checked with available experimental data. In cases for which discrepancies were found corrections were incorporated by curve fitting the difference between the available data and the model predictions (this was required for the viscosity and thermal conductivity of hydrogen). All property models and applicable corrections are provided in the Appendix. Comparisons of the modeled viscosity, conductivity, and diffusivity with experimental data (<http://webbook.nist.gov/chemistry/fluid/>) as a

function of temperature and pressure are presented in Figs. 1(a)–1(c), respectively. Figure 1(d) presents additional comparisons with the modeled constant pressure heat capacity derived directly from the equation of state²⁰ (also summarized in the Appendix).

The final properties requiring evaluation are the heat and mass diffusion factors. The Bearman–Kirkwood and the Irving–Kirkwood forms of the nondimensional thermal diffusion factors are related thermodynamically:

$$\alpha_{IK}^{(ij)} = \alpha_{BK}^{(ij)} + \frac{1}{\mathcal{R}T} \frac{M_i M_j}{M_m} \left(\frac{H_{,i}}{M_i} - \frac{H_{,j}}{M_j} \right), \quad (22)$$

where $H_{,i} = \partial H / \partial X_i$ is the partial molar enthalpy, and $\alpha_{IK}^{(ij)} = -\alpha_{IK}^{(ji)}$ and $\alpha_{BK}^{(ij)} = -\alpha_{BK}^{(ji)}$. Thus, only one factor needs to be specified as a property of the particular species pair. Following Refs. 22 and 23 we specify the “Irving–Kirkwood” form as a constant based on the molecular weight based correlation:

$$\alpha_{IK}^{(ij)} = 2.3842 \times 10^{-2} + 0.24821 \log_{10} \left[\max \left(\frac{M_i}{M_j}, \frac{M_j}{M_i} \right) \right]. \quad (23)$$

Of course, significant uncertainty exists in properly determining these parameters due to a lack of experimental data (particularly at high pressure). However, there are several reasons for the adopted approach. First, it has been shown that specifying $\alpha_{IK}^{(ij)}$ results in significant Soret effects and minimal Dufour effects. In contrast, the specification of $\alpha_{BK}^{(ij)}$ results in the opposite trend, in contradiction to previous low pressure findings that Dufour effects are nearly universally negligible. Second, the above procedure is consistent with the findings of Harstad and Bellan¹⁷ in comparing high pressure heptane droplet vaporization in nitrogen with experimental results. Third, previously reported high pressure parametric studies of the influence of varying α_{IK} for a binary species mixing layer showed that there is little effect of these variations over a relatively large range of α_{IK} values.¹⁸ Therefore, the effect of errors in assuming low pressure values should be minimal. Further work is, however, recommended in this area. Cross flame profiles of the resulting $\alpha_{BK}^{(ij)}$ are discussed below.

Finally, the mass diffusion factors, $\alpha_D^{(ij)}$, are modeled in a simplified manner by assuming ideal mixing behavior:

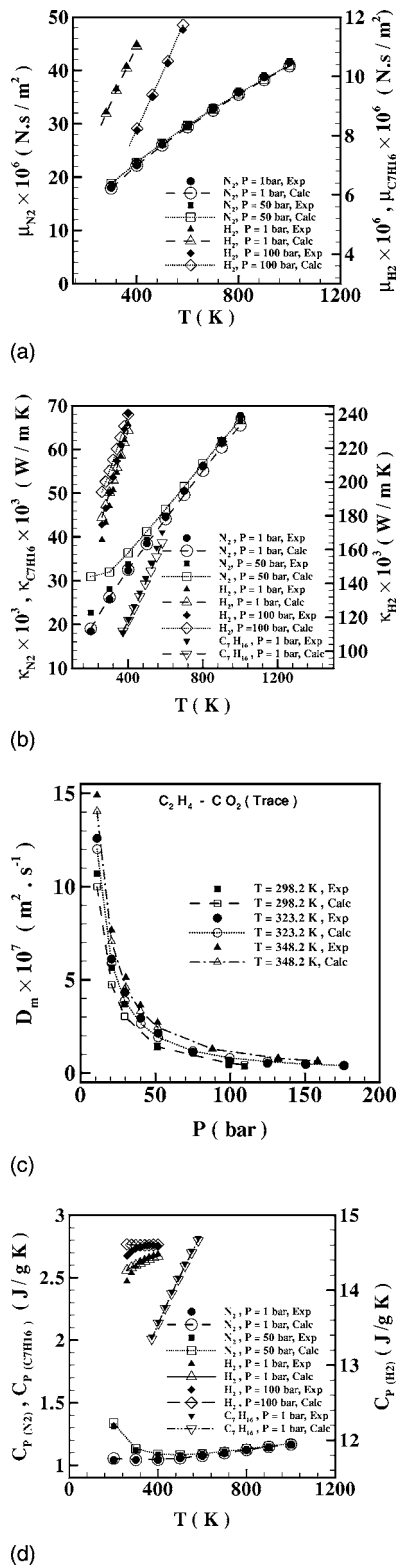


FIG. 1. Comparison of property models with experimental data: (a) viscosity, (b) thermal conductivity, (c) binary mass diffusion coefficient, and (d) heat capacity. All experimental data were obtained through the NIST web site: <http://webbook.nist.gov/chemistry/fluid/>, except for the mass diffusivities which are from Ref. 31.

$$\alpha_D^{(11)} = \alpha_D^{(22)} = 1, \quad (24)$$

$$\alpha_D^{(31)} = \alpha_D^{(32)} = -1, \quad (25)$$

$$\alpha_D^{(12)} = \alpha_D^{(21)} = 0. \quad (26)$$

In reality, the mass diffusion factors can be derived from the equation of state and are related to molar gradients of the mixture fugacity. Although the derivation exists for binary species, it becomes substantially more involved for larger numbers of species. We therefore follow the above approach as justified in Refs. 22 and 23 for conditions sufficiently “away” from the mixture critical locus. On the surface, this may be considered the “weakest” portion of the present modeling effort. However, we are using models for the actual temperature and pressure dependent mass diffusivities ($D_m^{(ij)}$) and have compared these property models with experimental data. Since these models and the high pressure experiments are almost undoubtedly assuming a Fickian form of the mass diffusion fluxes, it would be erroneous to use anything other than the ideal mixing values of the mass diffusion factors in conjunction with these properties. Consider, for example, a binary species system with a single mass flux vector: $J_i^Y = -\rho D_m \alpha_D \partial Y / \partial x_i$. Any model or experiment measuring D_m as the ratio of observed mass flux to the product of density and mass fraction gradient (i.e., without including α_D explicitly) would in actuality be measuring the product, $D_m \alpha_D$. In this case, clearly $\alpha_D = 1$ must be used with the measured mass diffusivity (i.e., variable α_D effects are included implicitly).

III. NUMERICAL APPROACH AND PROBLEM GEOMETRY

The fully compressible forms of the governing equations are solved for a simplified laminar diffusion flame geometry on a one-dimensional domain: $-L_2/2 \leq x_2 \leq L_2/2$. No incompressible or “low Mach number” approximations are employed in order to most accurately capture the correct flame evolutions, including any possible pressure gradient induced cross-diffusion effects. All spatial derivatives with respect to both x_1 and x_3 as well as the u_3 momentum equation are neglected. The resulting equations are solved numerically on a uniformly spaced mesh using the same parallel code employed in Refs. 22 and 23. The code is based on eighth-order accurate central finite differences for all spatial derivatives, fourth-order accurate Runge–Kutta time integration, and tenth-order accurate explicit filtering. Time steps are determined by minimum conditions imposed by both convective (including the acoustic velocity) and diffusive (for each of the kinematic viscosity, thermal diffusivity, and mass diffusivities) Courant numbers. These are set at 0.5 and 0.1, respectively. Validations of the code have been documented in Refs. 22 and 23 and have included reproduction of previously published low pressure results, reproduction of binary species results with the ternary species code, mass and energy conservation checks, energy spectra checks for isotropic turbulence simulations, comparison with property submodel predictions with experimental data (see Fig. 1), and extensive grid independence studies performed for all cases described in what follows.

For all simulations conducted for this work, the initial flow conditions are specified as follows. A binary species configuration is first chosen such that reactant species A occupies $x_2 > 0$ and reactant species B occupies $x_2 < 0$. Initial

TABLE II. Simulation parameters for the three reactions considered, $A+r_1B\rightarrow r_2C$: reaction number, reactant species A (species 1) and B (species 2), product species C (species 3), stoichiometric coefficients, ambient pressure, and number of grid points. All reactions have an initial temperature $T_0=700$ K, an initial “flame Reynolds number” $Re_F=1000$, and constant rate reaction Damkohler number $Da=1$. The heat release parameter is $Ce=2$ for the first two reactions and $Ce=5$ for the third reaction. Reactant A occupies $x_2>0$ and reactant B occupies $x_2<0$. All simulations are run both with and without Soret and Dufour diffusion.

Reaction	Reactant A	Reactant B	Product C	r_1	r_2	P_0 [atm]	N
1	Nitrogen	Oxygen	Nitric oxide	1	2	35	5000
2	Nitrogen	Dodecane	Heptane	0.4231	1	35	2000
3	Hydrogen	Oxygen	Water	0.5	1	100	1000

mass fraction profiles are “smoothed” using an error function profile along the centerline in order to allow for adequate resolution of spatial gradients: $\text{erf}(\pi^{1/2}x_2/\delta_0)$, where δ_0 is chosen to be the reference length ($L_0=\delta_0$) and represents an initial thickness for the flame. Note that other smoothing function choices exist, including the use of similarity profiles, however, results are only compared for each case between Soret/Dufour cases and those neglecting these effects. Therefore, the initial conditions are fixed for each case to better clarify the impact of including cross diffusion. Once the mass fraction profiles are specified, an initial uniform temperature and pressure are then applied with zero velocity throughout the entire domain, and the initial density is determined by the equation of state. At each time step temperature is calculated from the internal energy by means of a Newton–Raphson iterative procedure. Boundary conditions along the x_2 boundaries are nonreflecting outflow,³⁰ and the domain length varies for each simulation ($14.58\delta_0\leq L_2\leq 21.87\delta_0$).

As the primary focus of the current work is on molecular transport effects, and not on high pressure kinetics modeling, all simulated flames are chosen to be described by relatively simple one step, constant rate kinetics of the form $A+r_1B\rightarrow r_2C$. In order to both maintain consistency among the reactions and to ensure adequate resolution of all pertinent length and time scales (including diffusive and acoustic scales), each reaction is specified in terms of nondimensional parameters. For this purpose, a reference velocity scale is taken to be the average of the acoustic velocities (a) of the two free streams $\{U_0=[a(x_2=\infty)+a(x_2=-\infty)]/2\}$. Reference values for density $\{\rho_0=[\rho(x_2=\infty)+\rho(x_2=-\infty)]/2\}$, molecular weight $\{M_0=[M(x_2=\infty)+M(x_2=-\infty)]/2\}$, constant pressure heat capacity $\{C_{p,0}=[C_p(x_2=\infty)+C_p(x_2=-\infty)]/2\}$, and viscosity $\{\mu_0=[\mu(x_2=\infty)+\mu(x_2=-\infty)]/2\}$ are similarly chosen. Reaction rate constants and heats of reaction are then determined through specified values of the Damkohler number [$Da=K_R L_0 \rho_0 / (U_0 M_0)$] and the “heat release parameter” $\{[Ce=-\Delta H^0 / (T_0 C_{p,0})]\}$, respectively. Finally, the flame Reynolds number ($Re_F=\rho_0 U_0 L_0 / \mu_0$) is defined for the sake of convenience and its value is specified to be the same for all base case simulations, thereby determining the reference length (L_0) and actual physical domain length employed in each simulation. Physical domain length scales are typically $\sim 10^{-5}$ m.

IV. RESULTS

Three flames are considered in this study, with each simulation repeated once including Soret and Dufour cross diffusion, and again with standard Fickian and Fourier mass and heat diffusion as a base for quantifying the impact of the molecular transport model. Three specific reactions are chosen for simulation based on their relative molecular weights, relevance to modern combustion devices, and consistency with the present ternary species formulation. The particular reactions under consideration are of the form $A+r_1B\rightarrow r_2C$ and are listed in Table II. In all cases, reactant species A occupies $x_2>0$ and reactant species B occupies $x_2<0$. The first two reactions involve various hydrocarbons under thermodynamic conditions relevant to gas turbines and diesel engines ($P_0=35$ atm), whereas the third reaction is under conditions more relevant to rocket engines ($P_0=100$ atm). Note that reaction 2 is fictitious (as are the reaction rates and heat release values for all reactions) and is used only to consider the combustion of a heavy hydrocarbon with air to yield an intermediate molecular weight hydrocarbon under the present formulation. Note that the lack of molecular balance in reaction 2 is irrelevant as only species A , B , and C mass fractions are tracked (not individual atomic species) and the formulation is mass balanced and completely self-consistent. All three base case simulations described in Table II are performed twice; once including the complete transport formulation and a second time excluding Soret and Dufour diffusion effects. The latter is accomplished by nulling the cross diffusion fluxes: $Q_j^{Y1}=Q_j^{Y2}=Q_j^P=0$, $J_{j,1}^T=J_{j,1}^P=0$, and $J_{j,2}^T=J_{j,2}^P=0$. All thermal diffusion factors are additionally nulled: $\alpha_{IK}^{(ij)}=\alpha_{BK}^{(ij)}=0$. This reduces the formulation to standard Fourier and Fickian multispecies molecular transport. All base case simulations have an initially uniform temperature $T_0=700$ K with $Re_F=1000$ and $Da=1$. The base case heat releasing parameter was $Ce=2$ for reactions 1 and 2, and $Ce=5$ for reaction 3. Use of real diffusive properties puts extreme restrictions on the grid resolution required to resolve all pertinent length and time scales. For each flame simulation the grid size requirements were initially estimated based on the most restrictive diffusive property (initially estimated as $\Delta x_2=\alpha/U_0$ where α is the most restrictive diffusive property) and then carefully modified until all spurious oscillations were eliminated and grid independent results were obtained. Final grid resolutions used for the base case simulations are provided in Table II. Additional simulations

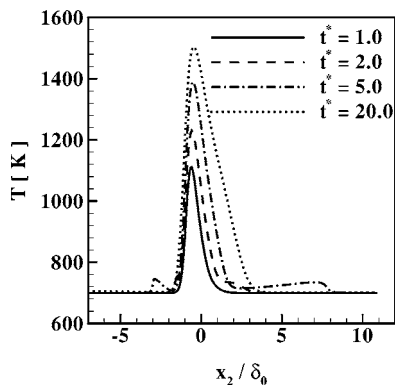


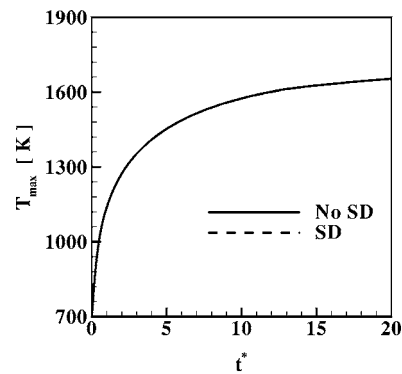
FIG. 2. Cross flame profiles of the temperature as a function of nondimensional time ($t^* = tU_0/L_0$) for reaction 3: $\text{H}_2 + \frac{1}{2}\text{O}_2 \rightarrow \text{H}_2\text{O}$ (including cross diffusion).

for the same reactions were also conducted for this study parametrically varying the flame Reynolds number, heat release parameter, Damkohler number, and the ambient pressure. Computational requirements varied significantly among the various cases, with the most restrictive case (reaction 1 at $P_0 = 35$ atm) requiring approximately 140 000 time steps and approximately 8 h running on 10 processors on a Pentium III based Beowulf cluster.

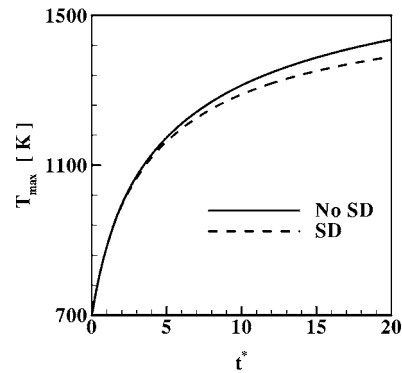
The temporal evolution of the simulated temperature distributions from a typical simulation is presented in Fig. 2. The results correspond to reaction 3 under the base case parameters described in Table II ($\text{H}_2 + \frac{1}{2}\text{O}_2 \rightarrow \text{H}_2\text{O}$), and include cross diffusion. Reactant A (hydrogen) occupies the $x_2 > 0$ portion of the domain, and reactant B (oxygen) occupies the $x_2 < 0$ domain. At the initial simulation time both the temperature and the pressure are uniform across the domain with $T_0 = 700$ K and $P_0 = 100$ atm, respectively. At this time an initially thin mixed reactant interface exists at $x_2 = 0$ due to the error function smoothing of the mass fraction profiles. The constant rate reaction is therefore relatively intense upon ignition. The various profiles presented in the figure correspond to different times quantified through the nondimensional variable $t^* = tU_0/L_0$ (i.e., time normalized by the characteristic acoustic time scale). Nonsymmetric temperature profiles are generated as the flame expands more readily into the lighter hydrogen stream. Peak temperatures rise quickly at early times, and then more slowly at later times with a maximum of approximately 1500 K at $t^* = 20$. An outgoing pressure wave is captured by the fully compressible flow simulations whose effects can be observed in the temperature profile at time $t^* = 5$ in the figure. Potential effects of combustion related pressure gradients are one reason that the complete cross-diffusion derivation including terms proportional to pressure gradients is considered in the present investigation.

A. Global impact of cross diffusion

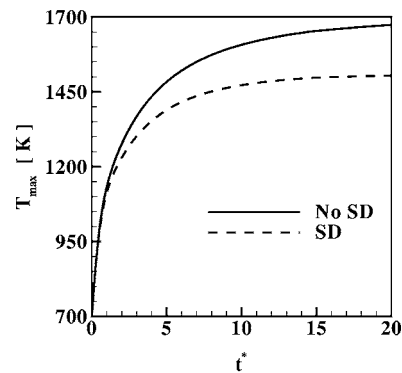
From an engineering perspective, it is crucial to gauge the ultimate impact of Soret and Dufour cross diffusion on observed bulk flame properties. For the present purposes these include the temporal evolutions of both the maximum



(a)



(b)



(c)

FIG. 3. Temporal evolution of the maximum flame temperature both with and without Soret and Dufour cross diffusion for base case (a) reaction 1, (b) reaction 2, and (c) reaction 3.

flame temperature and the measured flame thickness. These are provided in Figs. 3 and 4 for all three base case flames (see Table II). For present purposes, the flame thickness, δ_F , is calculated as the spatial distance spanned between locations where the product species mass fraction is equal to half of its instantaneous maximum value. Data are presented for both the complete heat and mass flux formulations, as well as for the reduced Fourier and Fickian forms as a reference for comparison. The maximum flame temperature is observed to rise rapidly during early times and then to reach a quasi-steady value at long times for all flames (Fig. 3). Similar trends are observed for the flame thickness (Fig. 4).

Previous results for pure binary^{20,21} and ternary^{22,23} species mixing in isotropic turbulence have shown that cross

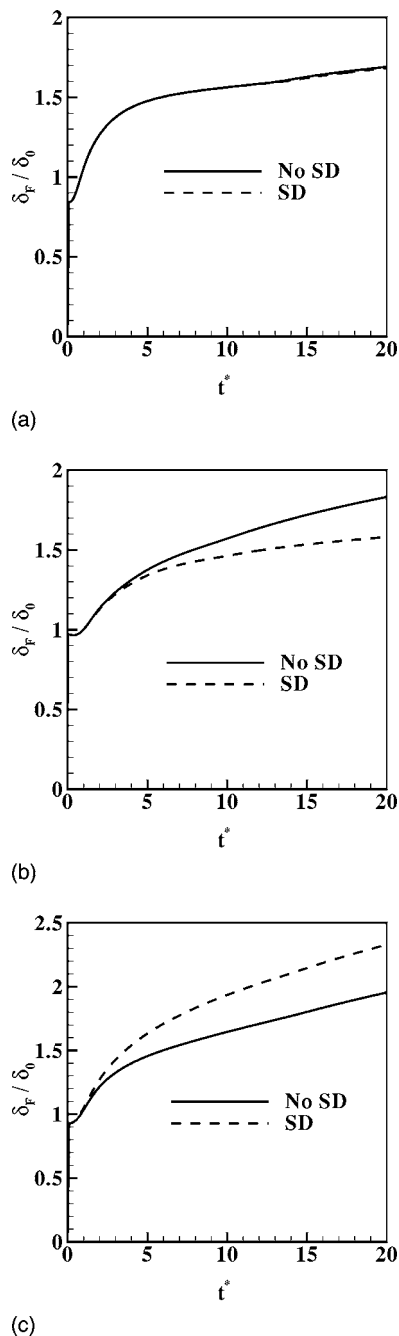


FIG. 4. Temporal evolution of the flame thickness both with and without Soret and Dufour cross diffusion for base case (a) reaction 1, (b) reaction 2, and (c) reaction 3.

diffusion, when significant, is maximized for species pairs having substantially varying molecular weights. This was attributed to enhanced partial molar volume (V_i) and partial molar enthalpy (H_i) differences appearing in the Soret diffusion terms. For the long time isotropic mixing Dufour effects were found to be negligible, and observed mixing variations were linked to pressure gradient Soret effects rather than to components proportional to the temperature gradient (no strong temperature gradients were present in these nonexothermic studies).

Similar molecular weight induced trends are confirmed for the presently addressed exothermic laminar diffusion

flames as evidenced in both Figs. 3 and 4. Reaction 1 contains N_2 , O_2 , and NO , which all have nearly identical molecular weights (see Table I). Differences between the complete molecular transport model and “standard” Fickian and Fourier models in the predicted bulk maximum temperature and flame thickness measurements are insignificant for this flame [Figs. 3(a) and 4(a)]. However, as the species involved in the reaction have increasingly varying molecular weights (reactions 2 and 3), substantial variations in both the maximum temperature and the flame thickness occur.

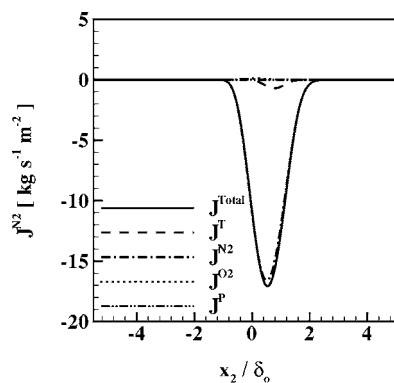
The inclusion of the complete cross-diffusion model results in final time peak flame temperature reductions of approximately 45 K and 169 K for the heavy hydrocarbon reaction (reaction 2) and the hydrogen/oxygen reaction (reaction 3), respectively. Even larger effects are found for the flame thickness (Fig. 4). Again, no significant alteration to the flame thickness is apparent for reaction 1, whereas maximal effects are evident for reaction 3. One interesting observation from these data is the fact that the flame thickness is decreased in the presence of Soret and Dufour diffusion for the hydrocarbon flame [reaction 2, Fig. 4(b)] but the opposite trend is found for the H_2/O_2 flame [reaction 3, Fig. 4(c)]. In order to explain this effect it is necessary to examine the actual heat and mass flux vectors and their respective components.

B. Mass and heat flux vector profiles

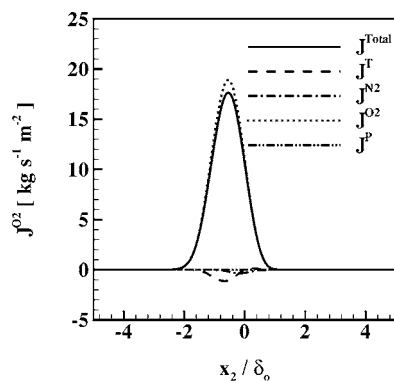
In order to elucidate the impact and the various contributions associated with the molecular transport terms, a complete set of heat and mass flux vector components is examined in Figs. 5–7 for reactions 1–3, respectively. The components of the diffusion vectors presented correspond to those proportional to temperature, concentration, and pressure gradients as described by Eqs. (7) and (8). The “total” diffusion vectors are also included which reveal the superimposed net effect of the individual component vectors. All profiles presented in these figures were obtained at the non-dimensional time $t^*=20$ and depict the inner portion of the domain surrounding the reaction zone. All vectors correspond to the x_2 components for this one-dimensional reaction.

In agreement with the results of the previous two figures, Fig. 5 indicates that Soret diffusion effects are nearly absent for reaction 1 as all three species involved have nearly equal molecular weights (N_2 , O_2 , and NO). Only a very small contribution from temperature gradient proportional mass flux (J^T) is detectable with the effect of slightly increasing the rate of N_2 diffusion into the flame zone, while slightly decreasing the rate of O_2 diffusion into the zone. Pressure gradient induced mass flux, and all Dufour effects on the heat flux vector are completely negligible.

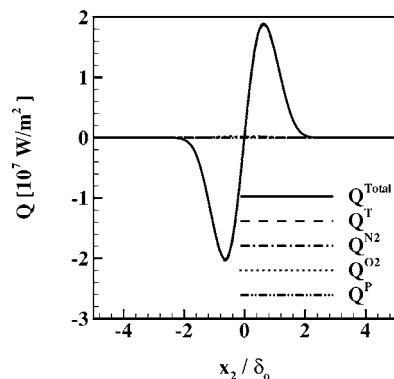
In contrast, reactions 2 and 3 involve species with increasingly varying molecular weights (N_2 , $C_{12}H_{26}$, and C_7H_{16} for reaction 2, and H_2 , O_2 , and H_2O for reaction 3). As is to be expected from our past findings, these reactions exhibit significantly increased cross-diffusion effects. Figure 6 presents the same flux component vector profiles for reaction 2. Soret diffusion effects are relatively strong for this reac-



(a)



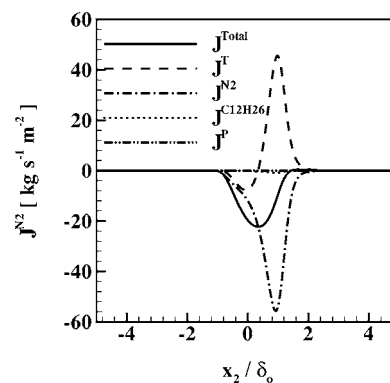
(b)



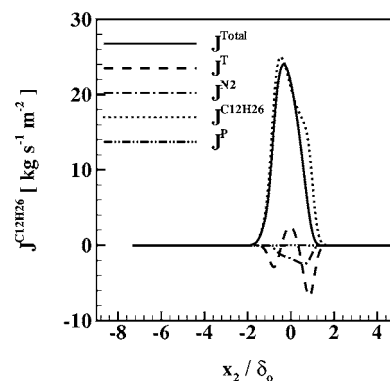
(c)

FIG. 5. Reaction 1 cross flame profiles of the (a) nitrogen mass flux vector, (b) oxygen mass flux vector, and (c) heat flux vector components at the final simulation time, $t^* = 20$.

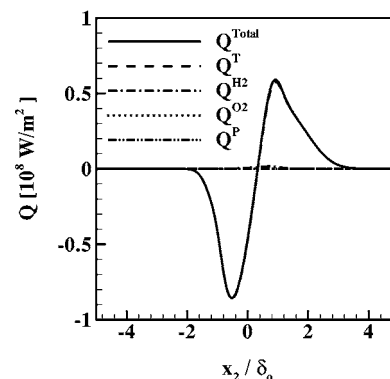
tion. The rate of molecular diffusion of both reactants into the reaction zone is reduced. In fact, for the lighter reactant, N_2 , the rate of mass flux is decreased by approximately 60% by the temperature gradient Soret flux. For nitrogen, both the pressure (J^P) and cross mass diffusion ($J^{C_{12}H_{26}}$) terms are negligible. However, a slightly different trend is observed for the heavier species, dodecane. In this case J^T and J^{N_2} both counteract the primary Fickian mass diffusion, with J^T also having small positive influence, resulting in an approximate 4% reduction in the total mass flux vector feeding the heavy fuel to the reaction zone. These reductions in mass flux rates manifest themselves in a reduced maximum flame temperature and flame thickness relative to cases involving purely



(a)



(b)



(c)

FIG. 6. Reaction 2 cross flame profiles of the (a) nitrogen mass flux vector, (b) dodecane mass flux vector, and (c) heat flux vector components at the final simulation time, $t^* = 20$.

Fickian mass diffusion [see Figs. 3(b) and 4(b)]. Dufour effects are also negligible for reaction 2 [Fig. 6(c)].

Corresponding mass and heat flux vectors are presented for reaction 3 (H_2 , O_2 , H_2O) in Fig. 7. For this reaction both the lighter (H_2) and the heavier (O_2) species are substantially affected by Soret diffusion. The oxygen mass flux rate [Fig. 7(b)] is reduced by approximately 50% with the primary Fickian flux (J^{O_2}) primarily opposed by both J^T and J^{H_2} . On either reactants "side" of the flame its own mass fraction gradient has an opposite sign as the local temperature gradient. There is, however, a small region of mass flux enhancement due to J^T for positive x_2 . This behavior can be ex-

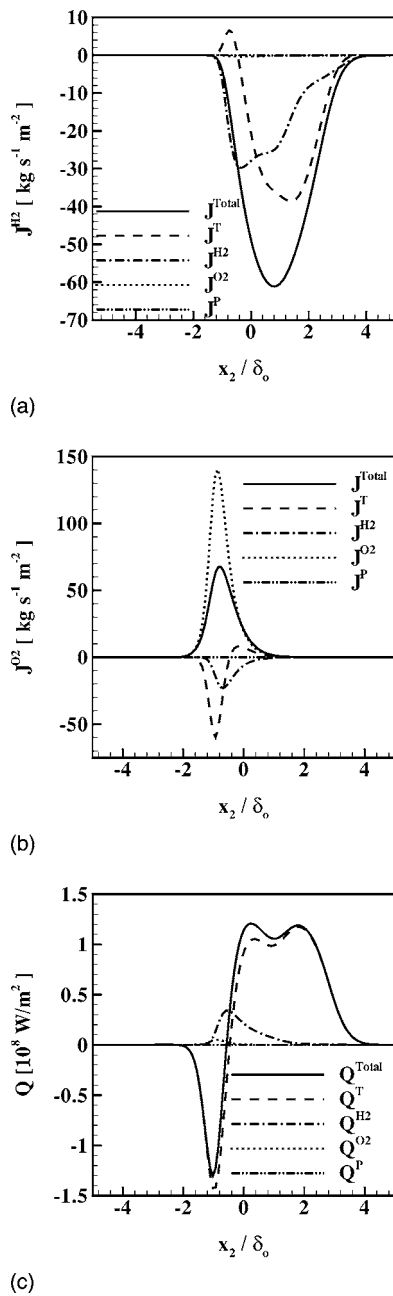


FIG. 7. Reaction 3 cross flame profiles of the (a) hydrogen mass flux vector, (b) oxygen mass flux vector, and (c) heat flux vector components at the final simulation time, $t^* = 20$.

plained based on the profiles of Bearman–Kirkwood thermal diffusion factor and temperature gradient ($\partial T / \partial x_j$) appearing in the J_j^T Soret flux [Eq. (20)].

In contrast, the rate of hydrogen mass transport is actually increased by the temperature gradient dependent Soret term, J^T [Fig. 7(a)]. The total mass flux vector is in this case approximately 50% larger in the presence of the Soret diffusion (again, a small region of opposite contribution occurs for negative x_2 regions). An explanation for this effect is given below in terms of the negative thermal diffusion factors for hydrogen. Irregardless of its explanation, the net effect of reduced O_2 transport and enhanced H_2 transport sheds light on the reaction 3 maximum temperature and flame

thickness evolutions presented previously in Figs. 3(c) and 4(c). Despite the increased availability of hydrogen, the reaction is limited by the reduced presence of oxygen and therefore exhibits a reduction in maximum temperature relative to the standard Fickian diffusion flame. In contrast, the increased diffusion of hydrogen results in the diffusion zone spreading relatively rapidly into the hydrogen free stream and therefore “appearing” much thicker (on the hydrogen side) than the purely Fickian case. This effect is apparent in the nonsymmetric temperature profiles presented in Fig. 2.

Dufour transport effects are maximized for reaction 3 [Fig. 7(c)] as indicated by a relatively small decrease of thermal transport from the flame front for negative x_2 values, and smaller enhancement of heat transport on the positive x_2 side. However, the magnitude of these alterations is relatively small and most likely negligible for typical engineering calculations. In addition, pressure gradient induced effects are negligible for both mass and thermal transport for reaction 3; as well as for reactions 1 and 2. Early time heat and mass flux vectors were also analyzed for this study and their trends are generally similar. In particular, even for a time $t^* = 1$ when pressure gradients are maximized due to the initial flame ignition all pressure gradient induced cross-diffusion terms were found to be negligible. These terms would then appear to be safely neglected for flame simulations and modeling, unless some other mechanism for maintaining stronger pressure gradients was present in the flow.

As mentioned above, the Soret induced mass transfer enhancement of the lighter species for reaction 3 (an opposite trend as that observed in reaction 2) can be explained in terms of the thermal diffusion factors. In both cases, these correspond to the Soret term $J_{j,1}^T$ whose relation is given by Eq. (16). The pertinent terms appearing on the right-hand side of this equation are $\alpha_{BK}^{(12)}$ and $\alpha_{BK}^{(13)}$. Profiles of all of the Bearman–Kirkwood thermal diffusion factors are presented in Fig. 8 for the three base case reactions at time $t^* = 20$. These factors are calculated from Eq. (22) where the various $\alpha_{IK}^{(ij)}$ are assumed to be “small” constants based on the molecular weight ratios of the involved species pairs [Eq. (23); see the discussion above]. The magnitude of the thermal diffusion factors is directly related to the relative difference in molecular weights of the species pairs involved through the partial molar enthalpy differences appearing in Eq. (22). The lighter species for reaction 2 (N_2) experiences a mass flux reduction due to the Soret term, and Fig. 8(b) shows that both $\alpha_{BK}^{(12)}$ and $\alpha_{BK}^{(13)}$ are positive throughout the domain where temperature gradients are not negligible. Temperature gradients are positive in the negative domain ($x_2 < 0$), and negative in the positive domain ($x_2 > 0$). Therefore, the Soret term slightly enhances the Fickian mass flux in the negative domain ($x_2 < 0$) and opposes significantly in the positive domain ($x_2 > 0$). However, for reaction 3, the lighter species (H_2) has strongly negative values for both $\alpha_{BK}^{(12)}$ and $\alpha_{BK}^{(13)}$ [Fig. 8(c)]. This characteristic of the partial molar enthalpy differences involving hydrogen manifests itself in Soret diffusion enhancing Fickian mass transport as was illustrated in Fig. 7(a).

Note that the above trend of hydrogen mass flux en-

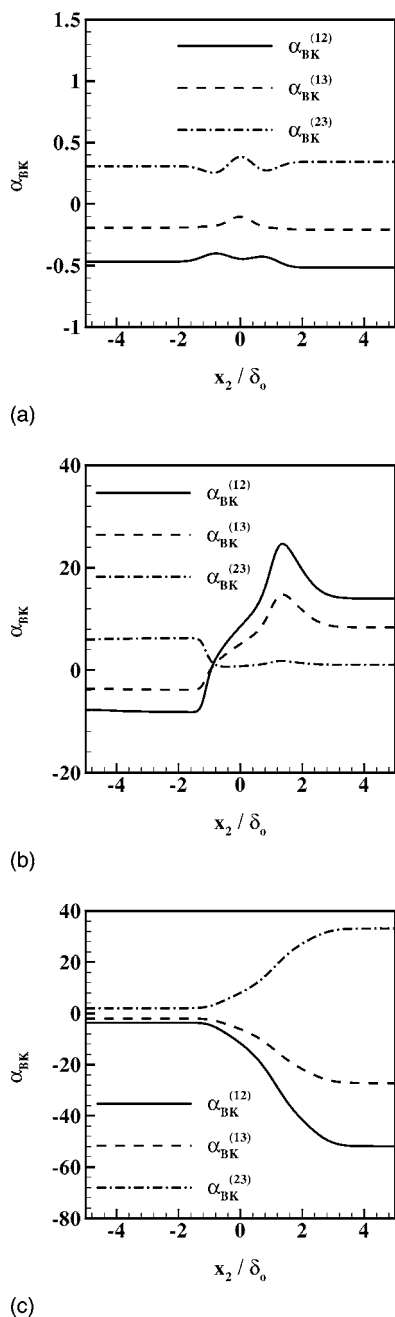


FIG. 8. Cross flame profiles of the Bearman-Kirkwood thermal diffusion factors for base case (a) reaction 1, (b) reaction 2, and (c) reaction 3 at time $t^* = 20$.

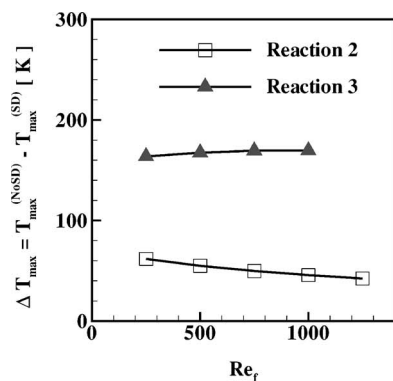
hancement by Soret diffusion should be considered to be an accurate result of the chosen model. However, there is indeed considerable uncertainty with respect to the proper specification of the Irving-Kirkwood thermal diffusion factor for these species and at these large pressures. As indicated above, prior spherically symmetric droplet simulations¹⁷ provide validation for the adopted approach through comparisons with high pressure experiments of heptane “droplets” diffusing in nitrogen. Considerable confidence, therefore, exists in the present approach for reaction 2 which displays trends similar to those of low pressure studies (as well as for reaction 1 which would not be expected to display significant Soret effects). On the other hand, the behavior of the thermal

diffusion factors for the hydrogen/oxygen/water system at large pressure could possibly be quite different. This could result in a sign change for the $\alpha_{BK}^{(ij)}$ factors and therefore yield Soret reductions in hydrogen mass transport. This would actually further increase the observed maximum temperature differences in comparison with the purely Fickian diffusion model, as the flame would be further starved of the hydrogen reactant. The present results would in this case serve as conservative estimates of the already large temperature reductions reported above for reaction 3 (although it would reverse the trends for the flame thickness due to reduction of the hydrogen diffusion rates). Note though that Irving-Kirkwood factors are $\sim 10^{-1}$. An increase of several orders of magnitude would be required to reverse the sign of $\alpha_{BK}^{(ij)}$ [see Eq. (22)]. The inverse treatment of these parameters, i.e., specifying the Bearman-Kirkwood form as a “small” constant, would also certainly alter the observed behavior. However, this would make Dufour effects substantial while minimizing Soret effects and would therefore not be expected (although it cannot be ruled out). Hopefully, findings such as these and other recently instigated research in high pressure mixing and combustion will lead to experimental research capable of answering such questions regarding hydrogen thermal diffusion factors.

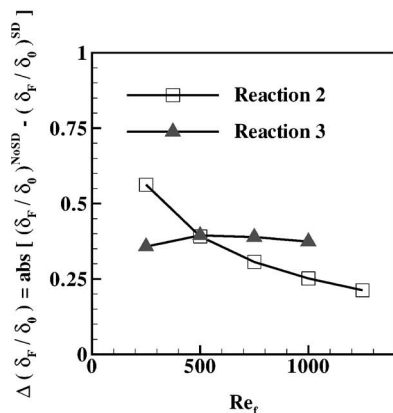
C. Effects of Re_F , Da , Ce , and P_0

Attention is now turned to generalizing the effects of cross diffusion on the global flame behavior. A parametric study was conducted for this purpose by performing a series of flame simulations for reactions 2 and 3 (reaction 1 had negligible effects) varying the flame Reynolds number (Re_F), the Damhohler number (Da), the heat release parameter (Ce), and the ambient pressure (P_0). All simulations are conducted at full resolution, and all are repeated for both the complete molecular transport and the purely Fickian and Fourier transport models. Results obtained from these parametric studies are presented in Figs. 9–12, respectively. These include the final time ($t^* = 20$) differences in the maximum temperatures and absolute differences in the measured flame thicknesses induced by cross diffusion. They therefore provide a direct quantitative measure of the global impact of cross diffusion on laminar flame modeling (under the restrictions of the simplified kinetics model employed). Each data point on these figures corresponds to the difference in the final time results of two complete simulations. The base case parameters are the same as those described previously: $Re_F = 1000$, $Da = 1$, for all three reactions. Base case heat releasing parameters are $Ce = 2$ for reaction 2, and $Ce = 5$ for reaction 3, respectively. The base case pressures are $P_0 = 35$ atm for reaction 2 and $P_0 = 100$ atm for reaction 3, respectively. Each of these is varied independently while keeping the remaining equal to their base case values.

The trends depicted in Figs. 9–12 reveal several characteristics of cross-diffusion effects on flame behavior. Reaction 3 (with more largely varying molecular weights) in all cases exhibits larger Soret induced temperature deviations in comparison to reaction 2. The maximum temperature devia-



(a)

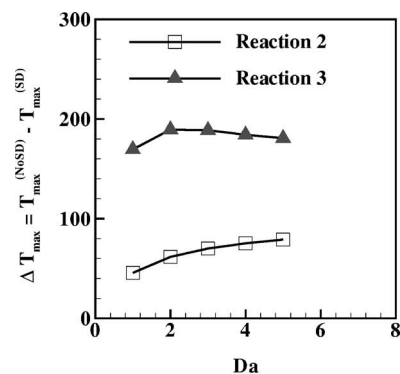


(b)

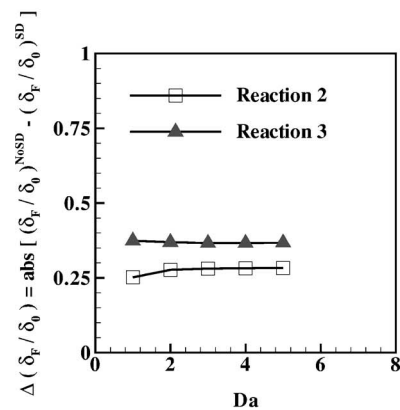
FIG. 9. Effects of the flame Reynolds number on the (a) maximum absolute flame temperature difference and (b) absolute flame thickness difference between simulations with and without Soret and Dufour diffusion at time $t^*=20$ for reactions 2 and 3. All simulations have fixed $Da=1$ with $P_0=35$ atm, $Ce=2$ for reaction 2 and $P_0=100$ atm, $Ce=5$ for reaction 3.

tions increased for reaction 3 and decreased for reaction 2 with increasing flame Reynolds number. Increases in the nondimensional reaction rate (Da) had an increasing influence of Soret induced maximum temperature differences for reaction 2. In contrast, reaction 3 displays a maximal temperature difference for $Da=2$ due to the increasing effects of thermal diffusion away from the reaction zone for larger reaction rates. Note that all trends depicted in these figures should be interpreted with respect to the fact that the physical length scale of the reactions is not fixed but is varied with the flow Reynolds number for each individual case and for each reaction. Finally, increasing the heat release parameter (Ce), causing larger peak flame temperatures, also increases the relative impact of cross diffusion.

The effect of the ambient pressure is more complex (Fig. 12). The ambient pressure is varied for each flame over pertinent ranges relative to each reaction. Reaction 3, being relevant to rocket engines, is varied over the range $1 \text{ atm} \leq P_0 \leq 200 \text{ atm}$. For reaction 2, being more relevant to gas turbine, diesel or gasoline fueled engines, the pressure is varied over the range $1 \text{ atm} \leq P_0 \leq 75 \text{ atm}$. As will be shown below, reaction 3 (H_2 , O_2 , H_2O) involves species which all behave essentially as ideal gases ($Z \approx 1$) under the conditions of this study. In contrast, the two hydrocarbons present in reaction 2 (heptane and dodecane) both exhibit significant



(a)



(b)

FIG. 10. Effects of the Damkohler number on the (a) maximum absolute flame temperature difference and (b) absolute flame thickness difference between simulations with and without Soret and Dufour diffusion at time $t^*=20$ for reactions 2 and 3. All simulations have fixed $Re_f=1000$ with $P_0=35$ atm, $Ce=2$ for reaction 2 and $P_0=100$ atm, $Ce=5$ for reaction 3.

compressibility, particularly near their critical pressures (see Table I). The mixture resulting from reaction 2 is therefore characterized by significant nonlinearity in the state equation, resulting in differing cross-diffusion behavior as a function of pressure. Reaction 3 shows monotonically increasing temperature deviations and monotonically decreasing flame thickness deviations with increasing pressure. In contrast, reaction 2 exhibits a peak in flame thickness deviation near the critical pressure of the mixture (note that these reactions are only simulated “near” the critical locus due to a supercritical temperature).

D. Density and compressibility profiles

Real gas compressibility and enhanced fluid density aspects of high pressure flames are addressed next. Profiles of both the mixture density and the compressibility, $Z = PV/(RT)$, are presented in Fig. 13 for each of the three base case flames at time $t^*=20$. Fluid densities are dramatically larger than typical low pressure gas flames with peak densities as large as approximately 260 kg/m^3 within the hydrocarbon (dodecane) stream of reaction 2 [Fig. 13(b)]. Reaction 1, comprised of species with near equal molecular weights, is characterized by a density minima along the reaction zone due to the enhanced flame temperature. In contrast, reactions 2 and 3 do not exhibit this characteristic as

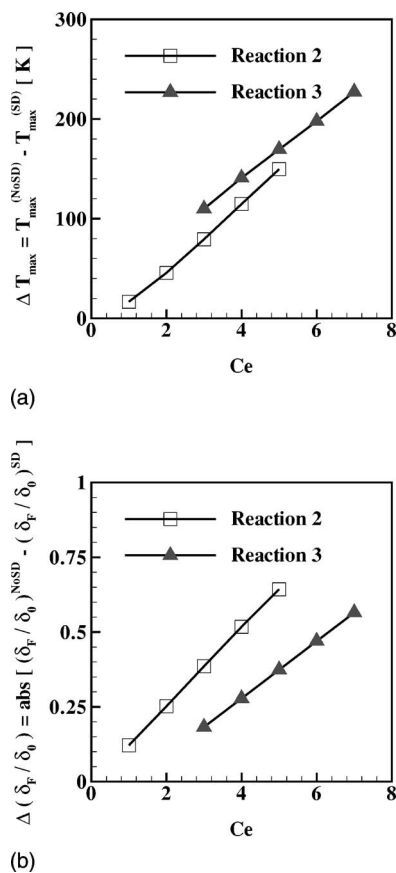


FIG. 11. Effects of the heat release parameter on the (a) maximum absolute flame temperature difference and (b) absolute flame thickness difference between simulations with and without Soret and Dufour diffusion at time $t^*=20$ for reactions 2 and 3. All simulations have fixed $Re_F=1000$ and $Da=1$ with $P_0=35$ atm for reaction 2 and $P_0=100$ atm for reaction 3.

the molecular weight of the mixture decreases continuously through the flame (along increasing x_2). The peak in the profile for reaction 3 [Fig. 13(c)] denotes an acoustic wave moving out of the domain. In regard to real gas effects, both reactions 1 and 3 have near unity compressibilities (nearly ideal gas behavior) throughout the entire domain. However, the hydrocarbon stream of reaction 2 [Fig. 13(b)] is characterized by near “liquid-like” Z values as small as $Z \approx 0.4$, and displays substantial real gas effects.

E. Prandtl and Schmidt number profiles

As mentioned below in the Appendix, high pressure property modeling is quite complex and relatively little experimental data exist. The models employed for the present study have been carefully chosen and corroborated with experimental data to the extent possible (see Fig. 1). It is therefore of interest to examine the nondimensional property profiles as illustrated by the mixture Prandtl and Schmidt numbers [$Pr = \mu C_p / \kappa_{\text{eff}}$ and $Sc_{m,ij} = \mu / (\rho D_m^{(ij)})$, respectively]. These profiles are presented in Fig. 14 for all three base case flame simulations at time $t^*=20$. Reaction 1 is very typical of low pressure gas behavior, with Prandtl and Schmidt numbers all nearly uniform across the domain and all less than unity. This same trend holds for the Prandtl numbers of the remaining reactions as well. In contrast, reactions 2 and 3

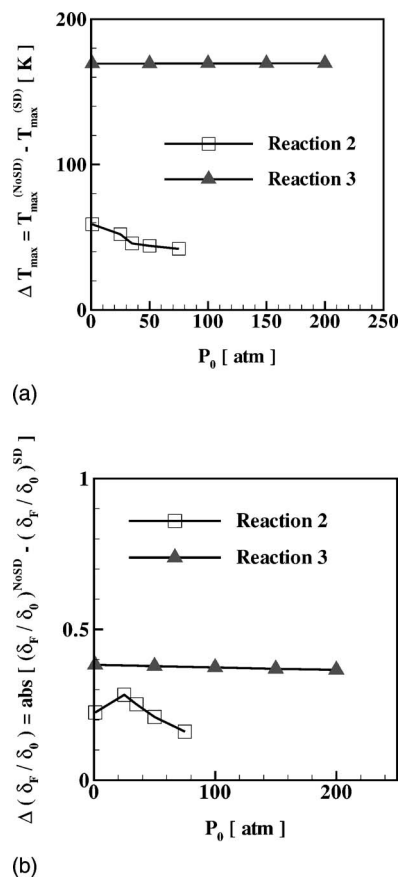


FIG. 12. Effects of the ambient pressure on the (a) maximum absolute flame temperature difference and (b) absolute flame thickness difference between simulations with and without Soret and Dufour diffusion at time $t^*=20$ for reactions 2 and 3. All simulations have fixed $Re_F=1000$, and $Da=1$ with $Ce=2$ for reaction 2, and $Ce=5$ for reaction 3.

yield substantially larger than unity values of the Schmidt numbers. The largest observed Schmidt numbers occur for the diffusion of dodecane into heptane for reaction 2, and for the diffusion of oxygen into water for reaction 3.

V. CONCLUSIONS

Direct numerical simulations have been performed for one-dimensional exothermic laminar diffusion flames at large pressures. The formulation includes the fully compressible form of the continuity, momentum and energy equations, together with a cubic real gas state equation. Heat and mass flux vectors as derived for a ternary species system from nonequilibrium thermodynamics and fluctuation theory describing Soret and Dufour cross diffusion are considered, including heat and mass flux terms proportional to temperature, concentration, and pressure gradients. Additional detailed models for the realistic temperature and pressure dependent mixture viscosity, thermal conductivity, heat capacity, and all binary mass diffusion coefficients are also included and validated through comparisons with experimental data. The governing equations were then solved using eighth-order accurate finite differencing for all spatial derivatives and fourth-order accurate time integration on a one-dimensional domain representing the laminar diffusion

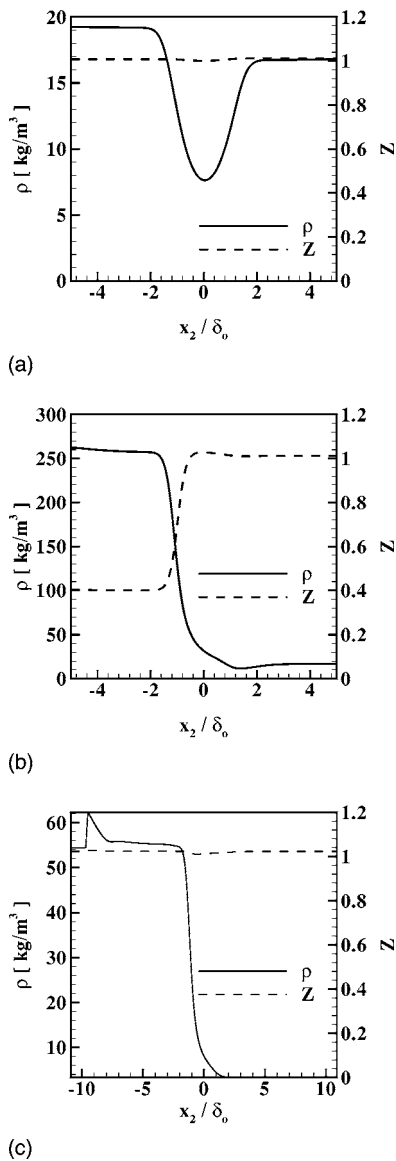


FIG. 13. Cross flame profiles of the mixture density and compressibility for base case (a) reaction 1, (b) reaction 2, and (c) reaction 3 at time $t^*=20$.

flame. The focus of the investigation was on a fundamental parametric study of molecular transport effects based on specified nondimensional flow parameters (the “flame Reynolds number,” Damkohler number, and heat release parameter), therefore, only relatively simple one step constant rate reactions conforming to the three species diffusion formulation were chosen. Although these restrictions negate direct quantitative assessment of actual chemical reactions, both the general trends with respect to these nondimensional parameters and the underlying physical explanations of how and why cross-diffusion effects occur in high pressure reactions are well characterized by the present study. All simulations were repeated for purely Fickian and Fourier mass and heat transport as a base with which to quantify the extent of cross-diffusion impact on the flame evolutions.

Three base case reactions were considered: (1) $N_2 + O_2 \rightarrow 2NO$ at $P_0=35$ atm, (2) $N_2 + 0.4231C_{12}H_{26} \rightarrow C_7H_{16}$ at $P_0=35$ atm, and (3) $H_2 + \frac{1}{2}O_2 \rightarrow H_2O$ at $P_0=100$ atm. All

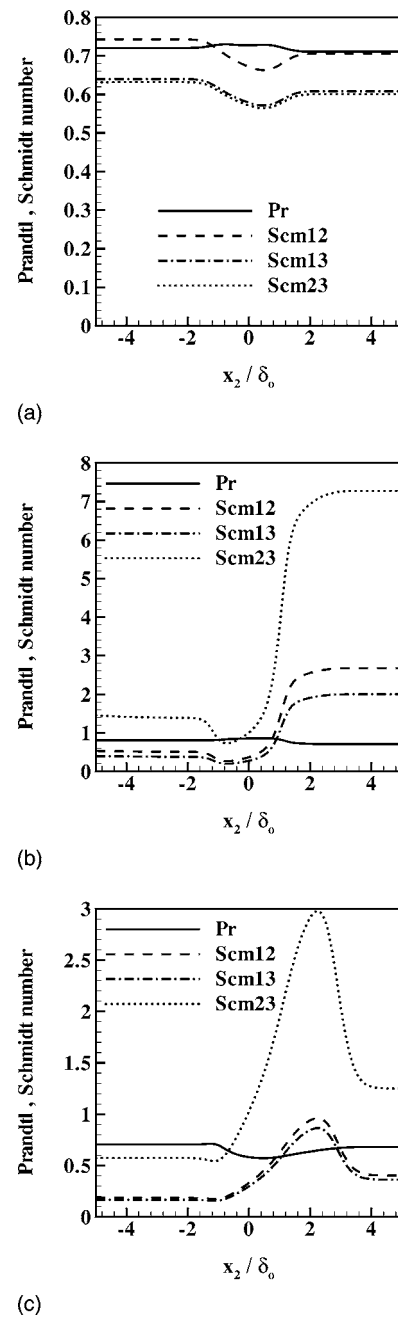


FIG. 14. Cross flame profiles of the mixture Prandtl and Schmidt numbers for base case (a) reaction 1, (b) reaction 2, and (c) reaction 3 at time $t^*=20$.

base case reactions further had a “flame Reynolds number” $Re_F=1000$, and Damkohler number $Da=1$. The nondimensional heat release parameter was $Ce=2$ for the first two reactions and $Ce=5$ for the third reaction. Each reaction was chosen based on the range of molecular weights of the species involved, relevance to various combustion problems, and conformity to the ternary species molecular transport model (the second reaction being purely hypothetical yet mass conserving). The results show that cross-diffusion effects become increasingly important for accurate flame simulations as the variability of the involved species’ molecular weights increases. Reaction 1, with nearly equal molecular weights, showed no evidence of significant Soret or Dufour

effects. However, for reaction 3 Soret diffusion was shown to result in an approximately ~ 200 K reduction in the maximum flame temperature (~ 100 K for reaction 2) in comparison with the purely Fickian and Fourier diffusion model. Large variations in the measured flame thickness were also attributed to Soret diffusion effects. Dufour heat transport was found to be essentially negligible for all cases. Observed behaviors were explained in terms of cross flame profiles for all of the heat and mass flux component vectors.

A parametric study was then conducted revealing that Soret induced flame deviations are generally increased with increasing Da and Ce , but are inversely related to Re_F . Effects of increasing pressure varied. The maximum flame temperature difference increased monotonically with increasing ambient pressure for reaction 3, comprised of nearly ideal gases. However, the hydrocarbons involved with reaction 2 behave as real fluids with maximum deviations from ideal gas behavior near their critical pressures. For this reaction Soret induced flame thickness differences were found to be maximized near the mixture critical pressure (≈ 25 atm). Finally, the mixture density, compressibility, Prandtl and Schmidt numbers were presented to further clarify the extent of real gas effects and the high pressure behavior of the property models.

The ultimate impact that cross diffusion will have on general engineering calculations will be dependent on the particular problem at hand. Temperature reductions due to Soret diffusion of order $\sim 100 \rightarrow 200$ K observed here have the potential to impact trace species concentration predictions, NO_x and other pollutant concentration predictions, and even engine fatigue and failure in modern gas turbines. The present results would therefore suggest that if such predictions are of importance, Soret mass diffusion due to temperature gradients (though not necessarily Dufour diffusion) may be required for accurate modeling efforts at high pressure. Although simplifying assumptions used in the present investigation preclude definitive conclusions regarding the actual quantitative effects of cross diffusion in real systems having hundreds of reactions and species, and temperature dependent reaction rates, the present results suggest a significant effect is potentially to be found. Individual species will still diffuse in a similar fashion in more complex systems and realistic transport properties have been used for all species relevant to high pressure reactions. Furthermore, instantaneous molecular diffusion is not affected by the form of the source term producing the flame temperature gradients (temperature dependent or otherwise). Therefore, qualitative trends documented in this study are expected to be retained in real high pressure flames. Nevertheless, inclusion of completely generalized molecular diffusion models in realistic combustion calculations will quite likely remain beyond the bounds of tractability for the foreseeable future. In this regard, “reduced” forms of the generalized heat and mass flux vectors more tractable to general engineering calculations are the subject of ongoing research and are beyond the bounds of the present investigation.

ACKNOWLEDGMENTS

This research was supported by the National Science Foundation through the Faculty Early Career Development Program; Grant No. CTS-9983762. All simulations were conducted on a parallel Beowulf PC cluster operated by the Department of Mechanical Engineering at Clemson University.

APPENDIX: PROPERTY MODELING

Models were sought for the temperature, pressure, and concentration dependent mixture viscosity (μ), thermal conductivity (κ), and binary species mass diffusion coefficients ($D_m^{(ij)}$). Only models based on the principle of corresponding states were considered in order to be applicable to arbitrary species given their molecular weights, critical properties, and acentric factors. Under the corresponding states theory all species will exhibit the same thermodynamic behavior when appropriate “reduced” variables are defined (i.e., when the temperature, pressure, volume and compressibility are normalized by their respective critical properties). Each model has its own recommended mixing rules for defining appropriate critical properties for a mixture. Model accuracy was additionally tested against experimental data where available, and any significant deviations were curve fit and added as corrections to the underlying models. For the present work corrections were only employed for the viscosity and thermal conductivity of hydrogen as described below. However, some of the models may require refinement for heavy hydrocarbons such as heptane. Only very limited high pressure data are available for these substances and we have not found sufficiently high temperature data with which to evaluate the accuracy for these species. Nevertheless, the chosen models will include correct trends as functions of temperature and pressure, and model accuracy would be expected to improve as temperatures increase and the fluids behave in a more gaseous manner.

Figure 1 presents various comparisons of the predicted species properties with experimental data as a function of both temperature and pressure. Final models were chosen based on recommendations of Reid *et al.*³ All model details (with the exception of the hydrogen curve fits and a high pressure mass diffusivity correction described below) can be found in Reid *et al.*³ However, as these are not always presented in that work as complete sets, the final model forms are repeated in their entirety in what follows. The formulation of the mixture heat capacity as calculated analytically from the equation of state is also included for the sake of completeness.

Viscosity

The “Lucas method” was employed to evaluate the mixture viscosity (μ) based on the following mixing rules for the mixture critical temperature, pressure, and molecular weight: $T_{cm} = \sum_i X_i T_{ci}$, $P_{cm} = \mathcal{R} T_{cm} (\sum_i X_i Z_{ci}) / (\sum_i X_i V_{ci})$, and $M_m = \sum_i X_i M_i$, respectively, where $Z = PV / (\mathcal{R}T)$ is the compressibility. The subscript cm denotes mixture critical properties and subscript ci refers to individual species critical proper-

ties. In this case, the “reduced” temperature and pressure are then $T_r = T/T_{cm}$, and $P_r = P/P_{cm}$, respectively. A reduced low pressure inverse viscosity, ξ , is then defined as

$$\xi = 0.176 \left(\frac{T_{cm}}{M_m^3 P_{cm}^4} \right)^{1/6}, \quad (\text{A1})$$

where T_{cm} is in degrees Kelvin, P_{cm} is in bars, and the units of ξ are $[10^{-7} \text{Ns/m}^2]^{-1}$ (the low pressure mixture viscosity is therefore $\mu^0 = 1/\xi$). High pressure mixture viscosities are then calculated by defining model parameters Z_1 and Z_2 . The first accounts for temperature variations:

$$Z_1 = [0.807T_r^{0.618} - 0.357 \exp(-0.449T_r) + 0.34 \exp(-4.058T_r) + 0.018]. \quad (\text{A2})$$

The parameter Z_2 accounts for pressure effects and is defined as

$$Z_2 = Z_1 \left[1 + \frac{aP_r^e}{bP_r^f + (1 + cP_r^d)^{-1}} \right], \quad (\text{A3})$$

which is valid for $1 < T_r < 40$ and $0 < P_r \leq 100$ (conditions applicable to the present study). Model parameters are evaluated as $a = a_1 \exp(a_2 T_r^\gamma) / T_r$, $b = a(b_1 T_r - b_2)$, $c = c_1 \exp(c_2 T_r^\delta) / T_r$, and $d = d_1 \exp(d_2 T_r^\epsilon) / T_r$. Numerical values used for the various parameters are $e = 1.3088$, $f = f_1 \exp(f_2 T_r^\zeta)$, $a_1 = 0.001245$, $a_2 = 5.1726$, $\gamma = -0.3286$, $b_1 = 1.6553$, $b_2 = 1.2723$, $c_1 = 0.4489$, $c_2 = 3.0578$, $\delta = -37.7332$, $d_1 = 1.7368$, $d_2 = 2.2310$, $\epsilon = -7.6351$, $f_1 = 0.9425$, $f_2 = -0.1853$, and $\zeta = 0.4489$. The high pressure corrected mixture viscosity is then $\mu = Z_2 / \xi$.

For certain species such as H_2 or He, the above procedure will be inaccurate without accounting for polarity or quantum effects. In the present investigation H_2 is used as one of the species. Rather than abandon the above approach, the predicted hydrogen viscosity was compared to experimental data from National Institute of Standards and Technology (NIST) (<http://webbook.nist.gov/chemistry/fluid/>). It was observed that the model predictions are in fact off by approximately 10% to 20%. However, the difference between the model and the data was predominantly only a function of temperature and not significantly altered at elevated pressures (i.e., the pressure correction in the model is accurate for hydrogen). Therefore, a curve fit was made to fit the difference which in practice is then added to the model prediction for hydrogen containing mixtures:

$$C_{\text{H}_2}^\mu = 0.0677563 + (2.505888 \times 10^{-3})T + (4.378022 \times 10^{-6})T^2 - (4.69188 \times 10^{-9})T^3 + (1.5502 \times 10^{-12})T^4, \quad (\text{A4})$$

where $C_{\text{H}_2}^\mu$ has units of $[\text{Ns/m}^2]$. For pure hydrogen $C_{\text{H}_2}^\mu$ is simply added to the model predicted viscosity. However, for mixtures, absent any experimental data, the correction is linearly superimposed: $\mu = \mu_{mod} + Y_{\text{H}_2} C_{\text{H}_2}^\mu$, where μ_{mod} is the uncorrected model predicted mixture viscosity and Y_{H_2} is the mass fraction of hydrogen in the mixture. The thermodynamic range over which the curve fit was validated is $200 \text{ K} \leq T \leq 1500 \text{ K}$, and $1 \text{ bar} \leq P \leq 100 \text{ bar}$.

Thermal conductivity

The thermal conductivity of the high pressure mixture is calculated in a similar fashion using the Steil and Thodos method.³ First, a new set of mixing rules is used as recommended: $T_{cm} = \sum_i \sum_j X_i X_j V_{cij} T_{cij} / V_{cm}$, $V_{cm} = \sum_i \sum_j X_i X_j V_{cij}$, $Z_{cm} = 0.291 - 0.08 w_m$, $w_m = \sum_i X_i w_i$, $P_{cm} = Z_{cm} \mathcal{R} T_{cm} / V_{cm}$, and $M_m = \sum_i X_i M_i$, where the individual species critical temperatures are $T_{cii} = T_{ci}$ and the additional critical temperatures for the mixing rules are $T_{cij} = (T_{ci} T_{cj})^{1/2}$. Similar terms for the molar volumes are $V_{cii} = V_{ci}$ and $V_{cij} = \frac{1}{8} [(V_{ci})^{1/3} + (V_{cj})^{1/3}]^3$. Based on these mixing rules, a low pressure mixture thermal conductivity (κ^0) is first defined by

$$\kappa^0 = \frac{\mu^0 C_{vm}}{M_m} \left[1.15 + \frac{2.03}{(C_{pm}/\mathcal{R}) - 1} \right], \quad (\text{A5})$$

in units of $[\text{W}/(\text{mK})]$ and μ^0 is the low pressure mixture viscosity defined above in units of $[\text{Ns}/\text{m}^2]$. The remaining variables are the constant pressure and the constant volume molar heat capacities; C_{pm} and C_{vm} , respectively (calculated from the equation of state with units of $[\text{J}/(\text{mole K})]$). Departure functions for the high pressure thermal conductivity (κ) are then defined as

$$\begin{aligned} (\kappa - \kappa^0) \Gamma Z_{cm}^5 &= 1.22 \times 10^{-2} [\exp(0.535 \rho_r) - 1], \quad \rho_r < 0.5, \\ (\kappa - \kappa^0) \Gamma Z_{cm}^5 &= 1.14 \times 10^{-2} [\exp(0.67 \rho_r) - 1.069], \quad 0.5 < \rho_r < 2.0, \\ (\kappa - \kappa^0) \Gamma Z_{cm}^5 &= 2.60 \times 10^{-3} [\exp(1.155 \rho_r) - 2.016], \quad 2.0 < \rho_r < 2.8, \end{aligned} \quad (\text{A6})$$

where

$$\Gamma = 210 \left[\frac{T_{cm} M_m^3}{P_{cm}^4} \right]^{1/6}, \quad (\text{A7})$$

and $\rho_r = \rho / \rho_{cm}$ is the reduced density and P_{cm} is in bars. As with the viscosity, a relatively poor model performance was found for hydrogen. In a similar fashion, deviations between the model and the experimental data were fit:

$$C_{\text{H}_2}^\kappa = 55.81329 - (0.1821439)T + (4.7057 \times 10^{-4})T^2 - (2.995339 \times 10^{-7})T^3 + (5.559443 \times 10^{-11})T^4, \quad (\text{A8})$$

and the final conductivity for mixtures containing hydrogen is calculated by adding $Y_{\text{H}_2} C_{\text{H}_2}^\kappa$ to the model predicted conductivity (in units of $[\text{W}/(\text{mK})]$). The thermodynamic range over which the curve fit was validated is again $200 \text{ K} \leq T \leq 1500 \text{ K}$, and $1 \text{ bar} \leq P \leq 100 \text{ bar}$.

Binary diffusion coefficients

Binary diffusion coefficients ($D_m^{(ij)}$) are modeled in a similar manner. First, the low pressure values ($D_{m,0}^{(ij)}$) are computed using the Fuller *et al.* method.³

TABLE III. Pure species low pressure constant pressure molar heat capacity [$J/(kg \cdot mole \cdot K)$] correlation coefficients from Reid *et al.*:³ $C_{p,\alpha}^0 = [C_1 + C_2 T + C_3 T^2 + C_4 T^3]$ with T [K].

Species	C_1	C_2	C_3	C_4
Nitrogen	3.115×10^4	-1.357×10^1	2.680×10^{-2}	-1.168×10^{-5}
Oxygen	2.811×10^4	-3.680×10^{-3}	1.746×10^{-2}	-1.065×10^{-5}
Nitric oxide	2.935×10^4	-9.378×10^{-1}	9.747×10^{-3}	-4.187×10^{-6}
Dodecane	-9.328×10^3	1.149×10^3	-6.347×10^{-1}	1.359×10^{-4}
Heptane	-5.146×10^3	6.762×10^2	-3.651×10^{-1}	7.658×10^{-5}
Hydrogen	2.714×10^4	9.274×10^0	-1.381×10^{-2}	7.645×10^{-6}
Water	3.224×10^4	1.924×10^0	1.055×10^{-2}	-3.596×10^{-6}

$$D_{m,0}^{(ij)} = \frac{0.001437 T^{1.75}}{P_{atm} M_{ij}^{1/2} [(\sum_v)_i^{1/3} + (\sum_v)_j^{1/3}]^2}, \quad (A9)$$

where the temperature is in [K], the atmospheric pressure is $P_{atm} = 1.01325$ bar, and $M_{ij} = 2[(1/M_i) + (1/M_j)]^{-1}$ is the mixing rule for the molecular weights of species i and j . The mass diffusivities resulting from the above have units [cm^2/s]. The additional terms appearing above, $(\sum_v)_i$, are obtained by summing atomic diffusion volumes for each species under consideration. Final values used for each species are provided in Table I. High pressure effects on the mass diffusion coefficients are included using the correlation proposed by Takahashi. However, this correlation is only presented as a graphical figure in Reid *et al.*³ (Fig. 11-3 of the citation). We therefore developed a curve fit for the high pressure correlation as a function of the reduced temperature and pressure [$f(T_r, P_r)$]:

$$f(T_r, P_r) = \frac{\exp(aP_r) + b}{(1+b)}, \quad T_r < 2.4,$$

$$f(T_r, P_r) = 1 + cP_r, \quad T_r > 2.4, \quad (A10)$$

where $a = (T_r - 2.4)/1.5$, $b = 6.2937T_r^2 - 9.0433T_r + 2.9334$, and $c = 0.015T_r - 0.036$, which matches the graphical correlation well. For this purpose the reduced mixture variables are defined as $T_r = T/T_{cm}$ and $P_r = P/P_{cm}$. The corresponding mixing rules suggested by Takahashi are used: $T_{cm} = \sum Y_i T_{ci}$ and $P_{cm} = \sum Y_i P_{ci}$. The final mass diffusion coefficients are then calculated as

$$D_m^{(ij)} = f(T_r, P_r) \frac{P_{atm}}{P} D_{m,0}^{(ij)}, \quad (A11)$$

with the pressure P again in units of [bars] and the resulting $D_m^{(ij)}$ again in units of [cm^2/s].

Heat capacity

The molar heat capacity of the mixture is calculated analytically from the Peng–Robinson equation of state:

$$C_p = C_p^0 - T \frac{(\partial p / \partial T)_{V,X}^2}{(\partial p / \partial V)_{T,X}} - \sum_{\alpha} X_{\alpha} \mathcal{R} - \frac{T \partial^2 \mathcal{A}_m / \partial T^2}{2\sqrt{2} \mathcal{B}_m} \ln \left[\frac{V + (1 - \sqrt{2}) \mathcal{B}_m}{V + (1 + \sqrt{2}) \mathcal{B}_m} \right], \quad (A12)$$

where C_p^0 is the low pressure reference heat capacity, A_m and B_m are the Peng–Robinson mixing parameters, and the remaining thermodynamic derivative terms have appeared in expanded form in Ref. 20. The correlations used for the C_p^0 are provided in Table III.

¹A. H. Lefebvre, *Gas Turbine Combustion* (Taylor and Francis, Ann Arbor, Michigan, 1999).

²R. D. Reitz and C. J. Rutland, "Development and testing of diesel engine CFD models," *Prog. Energy Combust. Sci.* **21**, 173 (1995).

³R. C. Reid, J. M. Prausnitz, and B. E. Poling, *The Properties of Gases and Liquids* (McGraw-Hill, Boston, 1989).

⁴J. Warnatz, U. Maas, and R. W. Dibble, *Combustion* (Springer-Verlag, Berlin, 1996).

⁵S. R. De Groot and P. Mazur, *Non-Equilibrium Thermodynamics* (Dover, New York, 1984).

⁶O. E. Tewfik, E. R. G. Eckert, and C. J. Shirliffle, "Thermal diffusion effects on energy transfer in a turbulent boundary layer with helium injection," in *Proceedings of the 1962 Heat Transfer and Fluid Mechanics Institute* (1962), pp. 42–61.

⁷O. E. Tewfik and J. W. Yang, "The thermodynamic coupling between heat and mass transfer in free convection with helium injection," *Int. J. Heat Mass Transfer* **6**, 915 (1963).

⁸E. W. Curtis and P. V. Farrell, "A numerical study of high-pressure droplet vaporization," *Combust. Flame* **90**, 85 (1992).

⁹A. Ern and V. Giovangigli, "Thermal diffusion effects in hydrogen-air and methane-air flames," *Combust. Theory Modell.* **2**, 349 (1998).

¹⁰A. Ern and V. Giovangigli, "Optimized transport algorithms for flame codes," *Combust. Sci. Technol.* **118**, 387 (1996).

¹¹A. Ern and V. Giovangigli, "Impact of detailed multicomponent transport on planar and counterflow hydrogen-air and methane-air," *Combust. Sci. Technol.* **149**, 157 (1999).

¹²D. E. Rosner, R. S. Israel, and B. La Mantia, "'Heavy' species ludwig-soret transport effects in air-breathing combustion," *Combust. Flame* **123**, 547 (2000).

¹³R. B. Dakhliya, V. Giovangigli, and D. E. Rosner, "Soret effects in laminar counterflow spray diffusion flames," *Combust. Theory Modell.* **6**, 1 (2002).

¹⁴K. G. Harstad and J. Bellan, "Isolated fluid oxygen drop behavior in fluid hydrogen at rocket chamber pressures," *Int. J. Heat Mass Transfer* **41**, 3537 (1998).

¹⁵K. G. Harstad and J. Bellan, "Interactions of fluid oxygen drops in fluid hydrogen at rocket chamber pressures," *Int. J. Heat Mass Transfer* **41**, 3551 (1998).

¹⁶K. G. Harstad and J. Bellan, "The Lewis number under supercritical conditions," *Int. J. Heat Mass Transfer* **42**, 961 (1999).

- ¹⁷K. G. Harstad and J. Bellan, "An all pressure fluid-drop model applied to a binary mixture: heptane in nitrogen," *Int. J. Multiphase Flow* **26**, 1675 (2000).
- ¹⁸R. S. Miller, K. G. Harstad, and J. Bellan, "Direct numerical simulation of supercritical fluid mixing layers applied to heptane-nitrogen," *J. Fluid Mech.* **436**, 1 (2001).
- ¹⁹N. A. Okong'o and J. Bellan, "Direct numerical simulation of a transitional supercritical binary mixing layer: Heptane and nitrogen," *J. Fluid Mech.* **464**, 1 (2002).
- ²⁰R. S. Miller, "Long time mass fraction statistics in stationary compressible isotropic turbulence at supercritical pressure," *Phys. Fluids* **12**, 2020 (2000).
- ²¹H. Lou and R. S. Miller, "On the scalar probability density function transport equation for binary mixing in isotropic turbulence at supercritical pressure," *Phys. Fluids* **13**, 3386 (2001).
- ²²H. Lou, Ph.D. dissertation, Clemson University, Department of Mechanical Engineering, 2002.
- ²³H. Lou and R. S. Miller, "On ternary species mixing and combustion in isotropic turbulence at supercritical pressure," *Phys. Fluids* **16**, 1423 (2004).
- ²⁴R. Hilbert, F. Tap, H. El-Rabii, and D. Thevenin, "Impact of detailed chemistry and transport models on turbulent combustion simulations," *Prog. Energy Combust. Sci.* **30**, 61 (2004).
- ²⁵B. Greenberg, "On the prediction of thermal diffusion effects in laminar one-dimensional flames," *Combust. Sci. Technol.* **24**, 83 (1980).
- ²⁶P. Garcia-Ybarra, C. Nicoli, and P. Clavin, "Soret and dilution effects on premixed flames," *Combust. Sci. Technol.* **42**, 87 (1984).
- ²⁷J. Keizer, *Statistical Thermodynamics of Nonequilibrium Processes* (Springer-Verlag, New York, 1987).
- ²⁸N. OKongo, K. Harstad, and J. Bellan, "Direct numerical simulations of O₂/H₂ temporal mixing layers under supercritical conditions," *AIAA J.* **40**, 914 (2002).
- ²⁹K. G. Harstad, R. S. Miller, and J. Bellan, "Efficient high pressure state equations," *AIChE J.* **43**, 1605 (1997).
- ³⁰T. J. Poinso and S. K. Lele, "Boundary conditions for direct numerical simulations of compressible viscous flows," *J. Comput. Phys.* **101**, 104 (1992).
- ³¹S. Takahashi and M. Hongo, "Diffusion coefficients of gases at high pressures in the system," *J. Chem. Eng. Jpn.* **15**, 57 (1982).